Journal of Hydrology 560 (2018) 301–317

Contents lists available at ScienceDirect

Journal of Hydrology

journal homepage: www.elsevier.com/locate/jhydrol

Research papers

On the origins of hypersaline groundwater in the Nile Delta aquifer

Joeri van Engelen [a,b,*], Gualbert H.P. Oude Essink [a,b], Henk Kooi [b], Marc F.P. Bierkens [a,b]

[a] Department of Physical Geography, Utrecht University, Heidelberglaan 2, 3584 CS Utrecht, The Netherlands
[b] Unit Subsurface and Groundwater Systems, Deltares, Daltonlaan 600, 3584 BK Utrecht, The Netherlands

ARTICLE INFO

Article history:
Received 21 September 2017
Received in revised form 8 March 2018
Accepted 12 March 2018
Available online 15 March 2018
This manuscript was handled by P. Kitanidis, Editor-in-Chief, with the assistance of Martin Thullner, Associate Editor

Keywords:
Nile Delta
Hydrogeology
Hypersaline
Brine
Groundwater

ABSTRACT

The Nile Delta is essential to Egypt's agro- and socio-economy. Although surface water is the traditional source for Egypt's irrigation, the shallow fresh groundwater resources underlying the delta are increasingly burdened by groundwater pumping, which increases interest in the status of the groundwater resources. Groundwater up to three times more saline than sea water was found at 600 m depth. The occurrence of this hypersaline groundwater raises doubts on the often-made assumption in the literature that seawater is the only source of salt in the Nile Delta aquifer and makes further investigation necessary. Knowledge on the origin of this hypersaline groundwater is key in assessing the possibility of deep fresh groundwater pockets. In this paper we conducted computational analyses to assess possible origins using both analytical solutions and numerical models. It is concluded that the hypersaline groundwater can either originate from Quaternary free convection systems, or from compaction-induced upward salt transport of hypersaline groundwater that formed during the Messinian salinity crisis. Our results also indicate that with groundwater dating it is possible to discriminate between these two hypotheses. Furthermore, it is deduced that the hydrological connection between aquifer and sea is crucial to the hydrogeological functioning of the Nile Delta Aquifer.

1. Introduction

The Nile Delta is essential to Egypt's agro- and socio-economy, as it constitutes most of the limited 3% of the country that is suitable for agriculture (WRI, 2008). Its wet and fertile lands have supported the Egyptian population for over 5000 years (Mączyńska, 2014), and currently host nearly 50 million inhabitants, making it the second most populated delta in the world, after the Bengal delta (Higgins, 2016). However, its fresh groundwater resources are suffering from agriculture increasingly relying on groundwater (Barrocu and Dahab, 2010) and a growing population (Bucx et al., 2010) that will further amplify extraction rates, making fresh water availability its most challenging issue for agriculture (FAO, 2005).

These stress factors have led to a continuous interest in available fresh groundwater resources and several studies on the topic. Kashef (1983) critically reviewed the available data, conducted water balance calculations, and estimated the extent of salt water intrusion with the Ghyben Herzberg relationship. He found several discrepancies in the available data, and concluded based on his water balance that at that time the aquifer was gaining fresh water. Despite this gain, he found that the extent of sea water intrusion was large. Sherif et al. (1988) constructed the first numerical groundwater model for the area, which was a 2D finite element model for variable density flow, also accounting for dispersion. Next to the large extent of sea water intrusion, the model showed that the width of the hydrodynamic dispersion zone could be considerable. Sefelnasr and Sherif (2014) created a 3D model and showed the sensitivity of the Nile Delta aquifer to sea level rise, as the shallow relief of the area resulted in a large extent of land surface inundation. Geirnaert and Laeven (1992) used hydrogeochemistry to reconstruct the paleohydrogeology of the area, up to 20,000 years BP, providing the first conceptual model for this period. They furthermore found that that the shallow groundwater in the center of the Nile Delta was recharged 3500 years BP as river water and in the bordering desert over 5000 years BP. Barrocu and Dahab (2010) extended this conceptual model up to 180,000 years BP, and further discussed the hydrogeochemistry. They concluded that the saline groundwater in the north is likely not in connection with the current sea, instead it is connate sea water, and further

Abbreviations: NDA, Nile Delta Aquifer; NDA-c, Nile Delta Aquifer compaction model; NDA-f, Nile Delta Aquifer free convection model; KES, Kafr El Sheikh formation.

* Corresponding author at: Department of Physical Geography, Utrecht University, Heidelberglaan 2, 3584 CS Utrecht, The Netherlands.
E-mail address: joeri.vanengelen@deltares.nl (J. van Engelen).

https://doi.org/10.1016/j.jhydrol.2018.03.029
0022-1694/

stress the fragility of the groundwater system. Despite that the previously discussed works increased our understanding of the system, we identify several research gaps: a) The numerical models made for this area do not take the paleohydrogeology in account, presumably due to computational limitations. b) Most studies implicitly assumed a completely open connection between aquifer and the sea, while this is uncertain. c) The studies mainly used data of the shallow groundwater system (roughly the upper 200 m of the upper aquifer), even though the upper aquifer is believed to extend up to 1000 m depth (Kashef, 1983; Sestini, 1989).

With increasing stress on the shallow groundwater system, interest in possible deeper fresh groundwater grows (Kang and Jackson, 2016). Therefore, the Egyptian Research Institute for Groundwater (RIGW) measured salinity at 200 m, 400 m and 600 m depth in 2013 and measured high values of Total Dissolved Solids (TDS) (Nofal et al., 2015) starting from 400 m depth at several locations (Fig. 1a), strongly suggesting a widespread occurrence of "hypersaline" groundwater at larger depths. No hypersaline groundwater was observed at 200 m depth. Given the interest in finding deeper fresh groundwater resources in the Nile Delta Aquifer (NDA, see Fig. 1b), a better understanding of the possible origins and transport of this hypersaline groundwater is necessary to assess further possibilities. "Hypersaline" groundwater is defined as groundwater exceeding the salinity of sea water (35 g/l) in this paper. Apart from the findings shown in Fig. 1a, two other observations of hypersaline groundwater in the NDA have been published. Firstly, Diab and Saleh (1982) found hypersaline groundwater near the shore, but did not report the depths of their samples. Secondly, there is the incidental remark by Shata (1999): "hot brine is recorded in oil wells at a depth of 1000 m below ground surface". As far as we are aware of, no other observations, hydrogeophysical or hydrogeochemical, have been published that reach 600 m depth, despite the multiple petroleum exploration wells that have been drilled, and logged, in the area.

Given the occurrence of this hypersaline groundwater, we question the often-made assumption that seawater is the only source of salt in NDA groundwater and deem further investigation necessary. Therefore, we test a number of plausible hypotheses on the origin of the NDA hypersaline groundwater using a combination of analytical solutions and numerical simulations. This analysis provides more insight into a) the timescales of salt transport involved in this large delta, b) which measurements should be collected to discern the origins of this hypersaline groundwater, and c) the possibility of deep fresh groundwater pockets. The goals of this study are to investigate the plausibility of a number of hypotheses (Listed in Section 3), to find a method to discriminate them in the field, and, where possible, falsify hypotheses.

Given the lack of study on this topic in this area, a brief summary of findings in other deltaic areas is warranted. As far as we are aware of, four other cases have been published that are relevant to this research. Firstly, hypersaline groundwater is found in fluvio-deltaic sediments near the Louisiana Gulf coast (Mississippi delta), which is probably the most well-studied area for this topic. Here, it is thought to originate from dissolution of salt domes brought upwards by thermal convection (Hanor and Mercer, 2011). Secondly, in the Netherlands (the Rhine-Meuse delta), hypersaline groundwater is found below the hydrogeological base, presumably caused by rock salt dissolution (Griffioen et al., 2016). Largely varying salinities are observed on the national scale, which can be partly explained by the presence of evaporite deposits and diffusive transport. Thirdly, high salinities found in the Burdekin Delta are explained by transpiration of mangroves and subsequent downward free convection (Fass et al., 2007). Fourthly, it is thought that intruded evapoconcentrated seawater is the cause of hypersaline groundwater near the Yellow River Delta (Han et al., 2011). In summary, these cases can be seperated into two groups: (1) those where hypersaline groundwater is thought to have originated from rock salt dissolution and (2) those where it is thought to be caused by evapoconcentration.

We argue here that these four cases are relevant to the Nile Delta, since evaporites are found below the hydrogeological base (Rizzini et al., 1978) and its climate provides ample opportunity for evapoconcentration. These processes will be discussed in further detail in section 3. The methods and findings of this research can also be applied to other deltaic areas overlying thick unconsolidated formations, such as the four previously mentioned

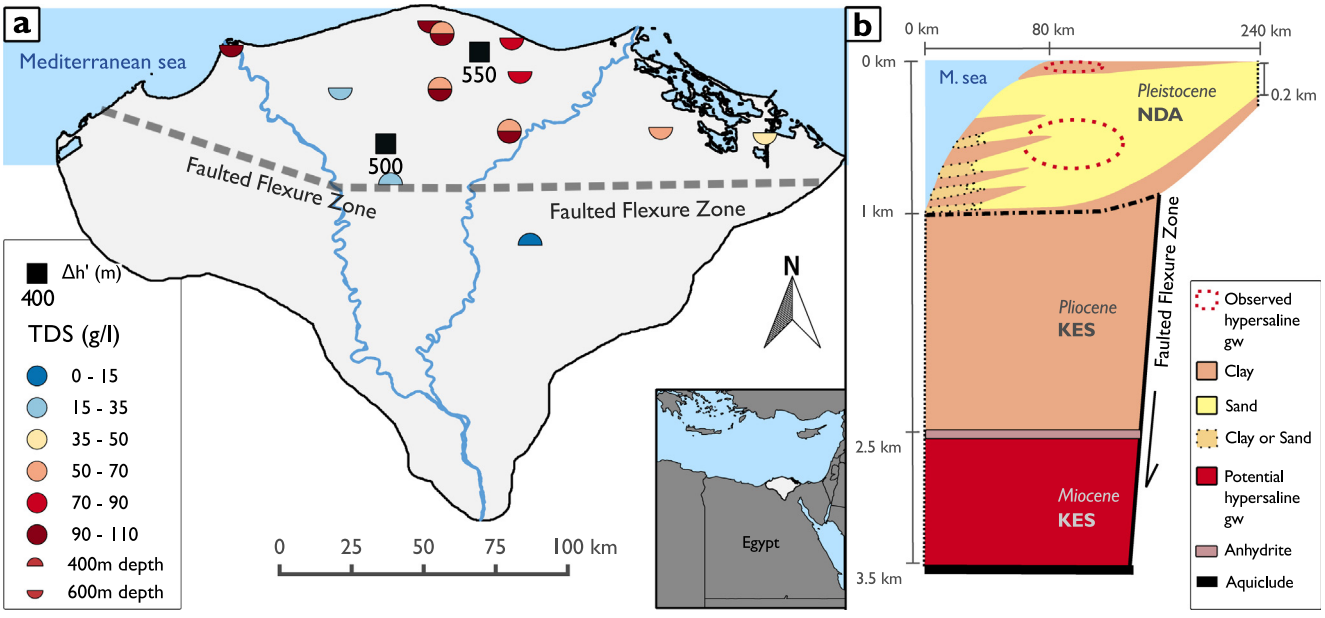

Fig. 1. (a): Total Dissolved Solids (TDS) measurements at 400 and 600 m depth in the Nile Delta (published previously by Nofal et al., 2015) and head difference (Δh′) over the anhydrite layer, expressed in freshwater head. The dotted black line represents the location of geological cross section. The map in bottom right corner shows the location of the Nile Delta in Egypt. (b): Sketched conceptual geological cross-section of the Nile Delta. The dash-dotted line indicates the boundary between separate model domains Nile Delta Aquifer (NDA) and Kafr El Sheikh formation (KES).

cases. Furthermore, they might be applied to cases where hypersaline groundwater might be found in the future, such as the Mekong Delta (Minderhoud et al., 2017), the Ganges-Brahmaputra Delta (Lindsay et al., 1991), and, in particular, the Niger Delta, which is geologically similar to the Nile Delta (Summerhayes et al., 1978).

2. Hydrogeological setting

A conceptual geological cross-section of the central NDA is shown in Fig. 1b. The NDA ranges in thickness from approximately 200 m near Cairo to 1000 m near the coast (Farid, 1980). It consists mainly of coarse Pleistocene sands and gravels, with some clay intercalations (Laeven, 1991). It is topped by a Holocene clay cap, ranging in thickness from 3 m at Cairo to a maximum of 100 m near the shore (Shata, 1999). In seismic studies, it is found that the bottom 750 m of the coastal boundary of the NDA is partially closed off by marine clays (Abdel Aal et al., 2000; Samuel et al., 2003; Abdel-Fattah, 2014), which is unaccounted for in previous groundwater research, though the existence of connections between the NDA and the sea is deemed possible in the form of conductive paleo-channels. There is an east-west trending fault system, "Fault Flexure zone", that presents a break in stratigraphy (Sestini, 1989) and causes an increase in thickness of the aquifer in northern direction. North of the fault flexure zone, the NDA is resting on top of a 1500 m thick formation consisting of mainly Pliocene marine clays (Sestini, 1989; Farouk et al., 2014) called the Kafr El Sheikh formation (KES). South of the fault flexure zone, the Nile Delta is underlain by limestones and shales ranging from Miocene to Oligocene age (Geirnaert and Laeven, 1992). Directly below KES, there is a 50 m thick layer of Messinian evaporites, consisting mainly of anhydrite (Rizzini et al., 1978). Below these evaporites, there is 1000 m of Miocene sands and conglomerates, underlain by compacted Miocene shales. Below these shales the pore pressures approach geostatic pressure (Nashaat, 1998), implying limited flow through the shales, therefore we assumed this serves as a hydrogeological base. Furthermore, we assumed the Fault Flexure zone is an impermeable boundary to flow, since 1) at larger depths there are several processes that can reduce fault horizontal permeability (Bense et al., 2013), such as clay smearing and particulate flow, and 2) offshore faults at similar depth clearly compartmentalize the subsurface, inferring from the high lateral differences in overpressure underneath the evaporate layer in Nashaat (1998).

3. Hypotheses

There are two possible origins of the hypersaline groundwater. Firstly, the hypersaline groundwater could originate from deeper deposits. We argue that it is certainly possible that hypersaline groundwater occurs in the 1 km thick Miocene layer, as evaporites are found up to the Fault Flexure Zone just underneath KES. These are correlated with the Messinian salinity crisis (Rizzini et al., 1978), during which the Mediterrenean sea reached high salinities and its water intruded bottom sediments. Some of this residual hypersaline water remained here (Vengosh et al., 1998). Furthermore, mud volcanos are found that seep hot brines originating from Messinian salt formations offshore at 3000 m water depth (Pierre et al., 2014). If hypersaline groundwater was transported upwards from deeper deposits onshore, it had to overcome resistance exerted by the high groundwater density and the low-permeable KES. There are three physical processes that can possibly overcome these resistances (Hanor, 1994; Person and Garven, 1994), namely 1) molecular diffusion (Domenico and Schwartz, 1990; Shackelford and Daniel, 1991a,b), 2) thermal driven free convection (Nield, 1968; Trevisan and Bejan, 1990; Nield and Bejan, 2013), as temperatures up to 90 °C have been observed underneath the KES (Riad et al., 1989) which may be associated with strong temperature gradients, and 3) upward solute transport driven by sediment compaction, since considerable overpressures have been measured onshore underneath the KES (Fig. 1a). These overpressures were likely caused by sediment loading, since the sedimentation rates during the Pleistocene and Pliocene were extreme (Nashaat, 1998), roughly 2500 m of deposits in 5.3 million years.

Secondly, it could originate from the top as the effect of 4) Holocene or Pleistocene free convection systems, originating from the evapotranspiration of sea or river water (Schreiber and Hsü, 1980; Wooding et al., 1997); similar to the cases in the Burdekin Delta and near the Yellow River Delta that were mentioned in Section 1 (Fass et al., 2007; Han et al., 2011). The high evapotranspiration rates in the Nile Delta of the past 10,000 years provide ample opportunity for the formation of hypersaline groundwater, deduced from the pockets of hypersaline groundwater found in the Holocene clay layer (Diab et al., 1997) and the hypersaline groundwater found underneath a sabkha neighbouring the Nile Delta (West et al., 1979). Stanley and Warne (1993) made a paleogeographical reconstruction of the past 30,000 years, showing several possibilities for hypersaline groundwater formation in this relatively short geological period. For example, sabkha muds (salt muds) were deposited in seasonally dry depressions between former channels from 30,000 to 11,500 years BP. Furthermore, the widespread wetlands of 6500–2000 years BP also at times transpired enough to create hypersalinity, inferred from the previously mentioned pockets of hypersaline groundwater in the Holocene clay (Diab et al., 1997). Another option might be a coastal lagoon that received little river water for a long period of time, such as during the early Holocene arid phase (Geirnaert and Laeven, 1992), analogue to the coastal sabkhas in the Northern Sinai (Gat and Levy, 1978).

We want to stress that this list of hypotheses is not exhaustive, due to the limited amount of data available at the depth of interest.

4. Methods

Computational analyses were conducted with either analytical solutions (hypotheses 1 and 2) or numerical models (hypotheses 3 and 4), to test the physical feasibility of mentioned four hypotheses. Since this is exploratory research, we tried to reduce the risk of incorrect hypothesis rejection as much as possible. Our ground rule was to set unconstrained parameters and boundary conditions in favor of the respective hypothesis under research, since constraining data was often scarce. If the hypothesis was then still falsified, we could then be quite certain that this process played no important role in bringing hypersaline groundwater to 600 m depth.

One assumption we made in this research affected our analyses for all hypotheses, namely we assumed NaCl as the sole source of salt, as this is the dominant salt in groundwater under natural conditions at TDS values up to 200 g/l (Hanor, 1994). At larger TDS values calcium becomes the more dominant cation, as groundwater gets saturated with respect to halite. This assumption affected both the molecular diffusion coefficient used, used for hypotheses 1–4, and the conversion from concentration to density, used for hypotheses 2–4. The effects of this assumption on our computational analyses are deemed unimportant, since the molecular diffusion coefficient of NaCl is higher than that of CaCl2 (Shackelford and Daniel, 1991a) thus not interfering with our ground rule, and the uncertainties introduced by a different linear equation of state are negligible compared to the other uncertainties in this research (Kohfahl et al., 2015).

4.1. Hypothesis 1: Analytical solution

Here we test whether molecular diffusion could have transported enough dissolved salts to explain the observed salinities upwards over the KES. Assuming no groundwater flow, solute-transport is purely governed by Fick's second law of diffusion in 1D (adapted for porous media), which is written as follows:

$$\frac{\partial C}{\partial t} = -D_c^* n_e \frac{\partial^2 C}{\partial z^2} \tag{1}$$

where C is the concentration of the solute (g/l), n_e the effective porosity (-), z the vertical distance (m), t is time (s), and D_c^* the effective diffusion coefficient (m^2/s). There is no general consensus regarding the exact definition of D_c^* (Domenico and Schwartz, 1990; Shackelford and Daniel, 1991a). In this study, we used values of Shackelford and Shackelford and Daniel (1991b), who defined

$$D_c^* = D_0 \tau_a \tag{2}$$

where D_0 is the molecular diffusion in free water at a certain temperature (m^2/s) and τ_a is an "apparent tortuosity" (-), which accounts for the combined effects of tortuosity, anion exclusion, and viscosity.

The following analytical solution to Eq. (1) describes the concentration development through the compacted clay through time:

$$C(z,t) = C_{max} + (C_{min} - C_{max})\mathrm{erf}\frac{z}{\sqrt{4D_c^* t}} \tag{3}$$

where C_{max} and C_{min} are the maximum and minimum concentrations respectively. We varied C_{max} in our analysis and set C_{min} to the TDS of seawater, which is 35 g/l. D_c^* was approximated by estimating τ_a. We used the highest values of D_c^* that we could estimate from the literature, in order to reduce the risk of incorrect hypothesis rejection. Shackelford and Daniel (1991b) rigorously conducted multiple experiments (8 test series) in triplicate at 25 °C for multiple species, of which they calculated the mean D_c^* of each test series. The highest mean D_c^* these authors found for Cl^- at 25 °C is 10.6e−10 m^2/s. Since D_0 of Cl^- at 25 °C is 20.3e−10 m^2/s (Shackelford and Daniel, 1991a), an upper limit for τ_a of 0.522 is inferred. In addition we corrected for temperature, as Riad et al. (1989) measured temperatures of 80 °C on average directly underneath the Kafr El-Sheikh layer at multiple points in the onshore Nile Delta. D_0 of NaCl at 80 °C is around 44e−10 m^2/s (Fell and Hutchison, 1971). Thus, assuming that τ_a for Cl^- is isotherm and is representative for NaCl, a D_c^* = 22.9e−10 m^2/s was used for compacted clay at 80 °C.

This hypothesis is rejected if filling in Eq. (3) with the most favorable parameters does not result in a concentration of 100 g/l at 1000 m depth (the top of the KES formation). This is the concentration that was observed at 600 m depth in the NDA.

4.2. Hypothesis 2: Rayleigh number for double diffusive convection

Here we will test thermal convection could have had its onset over the KES, which could subsequently transport dissolved salts upwards. Assuming initially stagnant groundwater and a homogeneous, isotropic aquitard, the onset of free convection over the KES formation was investigated by calculating the double-diffusive Rayleigh number (Nield, 1968; Trevisan and Bejan, 1990) and comparing it to its critical boundary:

$$Ra_t + Ra_c = Ra_t + Ra_t NLe > Ra_{crit} \tag{4}$$

With:

$$Ra_t = \frac{kgH\zeta_t \Delta T}{D_t \nu} \tag{5}$$

$$Ra_c = \frac{kgH\zeta_c \Delta C}{D_c^* \nu} \tag{6}$$

$$N = \frac{\zeta_c \Delta C}{\zeta_t \Delta T} \tag{7}$$

$$Le = \frac{D_t}{D_c^*} \tag{8}$$

$$\zeta_t = -\frac{1}{\rho}\frac{\partial \rho}{\partial T} \tag{9}$$

$$\zeta_c = -\frac{1}{\rho}\frac{\partial \rho}{\partial C} \tag{10}$$

where Ra_t is the thermal Rayleigh number, Ra_c the compositional Rayleigh number, Ra_{crit} the critical Rayleigh number; the rest of the parameters is explained in Table 1. These are extreme parameters, all chosen to maximize Ra_t and Ra_c, to minimize the risk of incorrect hypothesis rejection. It should be noted that Ra_t and Ra_c become negative when temperature or concentration gradients act stabilizing (Trevisan and Bejan, 1990); in this case Ra_c is negative. When $Ra_t + Ra_c > Ra_{crit}$, the groundwater system in the KES becomes unstable and free convection is possible. The value of Ra_{crit} depends on the chosen type of boundary conditions; in this case a fixed head, concentration, and temperature on top, and a no flux boundary and a fixed temperature and concentration at the bottom, gives $Ra_{crit} = 27.10$ (Nield, 1968; Trevisan and Bejan, 1990). The hypothesis is rejected if $Ra_t + Ra_c \ll Ra_{crit}$

4.3. Hypotheses 3 & 4: Numerical models

4.3.1. General approach

The variable-density solute transport code SEAWAT (Langevin et al., 2007) was used to simulate the development of TDS-fields,

Table 1
Limits of parameters chosen to fill in double diffusive convection analysis.

Symbol	Description	Value	Unit	Source
k	Permeability	4.80e−16	m^2	Table 3.2 in Domenico and Schwartz, 1990
g	Gravitational acceleration	9.81	m/s^2	
H	Thickness of clay layer	1500	m	Rizzini et al. (1978)
ζ_t	Volumetric thermal expansion coefficient (at 100 °C and 250 bar ~ 2500 m depth)	7.20e−4	1/°C	Beaton et al. (1987)
ζ_c	Volumetric compositional expansion coefficient	−7.14e−4	g/l[1]	Guo and Langevin (2002)
ΔT	Temperature difference over clay layer	70	°C	Riad et al. (1989)
ΔC	Assumed concentration difference over clay layer	65	g/l	Nofal et al. (2015)
D_t	Thermal diffusivity of clay	8.53e−7	m^2/s	Eppelbaum et al. (2014)
D_c^*	Effective molecular diffusion coefficient of clay	22.9e−10	m^2/s	See Section 4.1
ν	Kinematic viscosity of water	2.899e−7	m/s^2	Beaton et al. (1987)

pore pressures, and groundwater age within a cross-sectional domain up to 1 km depth representing the NDA (Fig. 1b). All of the models described in this paper were built with the Flopy package (Bakker et al., 2016). Groundwater ages were modeled directly, as first implemented by Voss and Wood (1993) and later extensively supported by Goode (1996), by adding "age" as an extra species with a constant production rate (Zheng, 2010).

SEAWAT solves the following governing equation for flow:

$$-\nabla \cdot (\rho \vec{q}) + \bar{\rho} q_s = \rho S_p \frac{\partial P}{\partial t} + n_e \frac{\partial \rho}{\partial C} \frac{\partial C}{\partial t} \tag{11}$$

With:

$$S_p = (\beta_p (1 - n_e) + n_e \beta_w) \tag{12}$$

And for solute transport:

$$\frac{\partial C}{\partial t} = \nabla \cdot (D \cdot \nabla C) - \nabla \cdot \left(\frac{\vec{q}}{n_e} C \right) - \frac{q_s}{n_e} C_s + \sum_{i=1}^{N} R_i \tag{13}$$

where ρ is the density of groundwater (kg/m^3), $\bar{\rho}$ is density of water entering through a source or leaving through a sink (kg/m^3), $\vec{q}$ is the specific discharge vector (m/d), q_s is the source/sink term (d^{-1}), P is the pore pressure (N/m^2), t is time (d), S_p is the specific storage in terms of pressure (m^2/N), β_p and β_w are the compressibility of the pores and water (m^2/N), respectively, C is the salt concentration (g/l), C_s is the source concentration (g/l), D is the hydrodynamic dispersion coefficient (m^2/d) R_i is the rate of solute production or decay in reaction i of N different reactions, and n_e is the effective porosity (−). For an elaborate explanation of Eqs. (11)–(13), the reader is referred to the SEAWAT manual (Guo and Langevin, 2002).

Boundary conditions were varied to either model salt input by compaction-driven inflow from below (NDA-c model) or free convection from the top (NDA-f model). These models evaluate hypotheses 3 and 4 based on their ability to approach the observed TDS at several points at 600 m. A separate model for the "KES" domain (1–3.5 km depth) was developed to produce the basal boundary condition of the NDA-c model. This sequential, "split-domain" approach (first KES, then NDA-c) was chosen to maintain practicable computation times, which ranged from half a day (KES model) up to a week (NDA-c model, with open coastal boundary). These large differences in computational times were caused mainly by the solute transport solver (MT3DMS), which based its time step internally on the maximum velocity in the model domain (Zheng and Wang, 1999). The NDA model had the highest velocities, while the KES model had a larger number of cells. Therefore, combining model domains would seriously burden simulation times, as this would result in three times the number of cells of the NDA model, with the same small time steps, causing maximum predicted model simulation times of three weeks per simulation. The sequential split-domain approach is reasonable since groundwater flows predominantly upwards from KES into NDA.

4.3.2. Methodological aspects of the numerical models

The NDA numerical models spanned 240 km by 1 km, the KES model 180 km by 3 km, and all models were discretized into cells of 1000 m (horizontal) by 10 m (vertical) (see also Fig. D1 for a grid convergence test). The time domain of the models ranged from 120.000 years (NDA-f) up to 2.5 million years (KES & NDA-c). The latter time domain implies we assume no overpressure build-up during the Pliocene in the KES formation.

4.3.2.1. KES model. To quantify volumetric flow and solute transport within the KES depositional strata during the Pleistocene and, in particular, the outflow at the top of this formation, we used a modified version of Bear (1972) partial differential equation for mass conservation in a deformable porous medium with external loading (his equation 6.3.26).

$$-\nabla \cdot (\rho \vec{q}) + \rho \beta_p \left(\frac{\partial \sigma}{\partial t} - \frac{\partial P}{\partial t} \right) = \rho n_e \beta_w \frac{\partial P}{\partial t} + n_e \frac{\partial \rho}{\partial C} \frac{\partial C}{\partial t} \tag{14}$$

where σ is the total stress or confining pressure (m^2/N), which is a function of sediment loading, and $\beta_p(\partial\sigma/\partial t - \partial P/\partial t) = \partial\varepsilon/\partial t$ is the strain rate of the porous medium (d^{-1}).

The applied modifications to Bear's original equation, which allow the equations to be solved with SEAWAT without any modifications to the original code, were a) the addition of the last term which allows local groundwater mass change due to change in salt content and b) the use of Eulerian (fixed space coordinates) rather than Lagrangian (relative to moving solids) time derivatives. The latter modification reflects the fact that we solve for pore pressure, TDS, and flows on a rigid model domain (present-day compressed state) and neglect temporal changes of vertical grid spacing and domain height associated with the compaction. This is considered reasonable as it yields conservative, underestimated magnitudes of the compaction-driven flow.

To solve Eq. (14) in SEAWAT, three variables of Eq. (11) were altered: S_p, q_s, and $\bar{\rho}$. Firstly, whereas normally $S_p = (\beta_p(1 - n_e) + n_e\beta_w)$ (Eq. (12)), in the KES model $S_p = n_e\beta_w$ (Eq. (14)). This required no modifications to the original code, as SEAWAT takes S_p as an input parameter directly.

Secondly, the strain rate, which equals the volumetric source term q_s in Eq. (11), was specified to be constant in the model, proportional to a constant Pleistocene sedimentation rate and constant pore compressibility.

$$q_s = \beta_p \left(\frac{\partial \sigma}{\partial t} - \frac{\partial P}{\partial t} \right) \approx \beta_p \left(\rho_b g \frac{\partial z_b}{\partial t} - \rho_w g \frac{\partial z_b}{\partial t} \right) = \beta_p (\rho_b - \rho_w) g \frac{\partial z_b}{\partial t} \tag{15}$$

where ρ_b the bulk density of the sediment, ρ_w the density of fresh water (kg/m^3), and $\frac{\partial z_b}{\partial t}$ the sedimentation rate (m/d). Eq. (15) approximates the temporal change of pore pressure to equal a hydrostatic pressure change ($\partial P = \partial P_h$) as the depth of the KES strata relative to the water table increases during burial. This overestimates the compression during early phases of Pleistocene sedimentation when excess pore pressures increase, but this overestimation becomes negligible after a short time as excess pore pressures stabilize. The validity of this approach is shown in Appendix C.q_s is constrained by the fact that the total amount of expelled pore water cannot exceed the pore water volume at time of deposition, and the latter can be approximated a priori by:

$$V_s = \int_{t_0}^{T} q_s \mathrm{d}t \leqslant n_{init} \tag{16}$$

where V_s is the total volume of water expelled from the pores relative to the initial bulk volume (−), or total strain, t_0 and T are the beginning and the end of the time domain (d), respectively, and n_{init} is the initial porosity (−), just after sediment deposition. With the parameters chosen in this research (Table 2), V_s equaled 0.26 and 0.13 for the Pliocene clay and Miocene deposits, respectively. We consider this an upper limit of the total water expelled by the pores during the Pleistocene.

Thirdly $\bar{\rho}$, the density of the water injected in a cell by q_s, had to equal the current concentration of the cell. This was determined by SEAWAT internally by using the "recirculation well option" of MT3DMS (Zheng, 2010). To ensure convergence, the maximum number of outer iteration steps of the dispersion solver (GCG) was set at 10 (the default value is 1). In practice, no more than three outer iterations were required for convergence.

The upper boundary of the KES model was a Cauchy boundary condition, of which the fresh water head is set at zero. To incorporate the effects of deposition of NDA sediments on this upper boundary, namely that the distance to the fixed head boundary

Table 2
Parameters chosen for the KES model. We are purposely inconsistent with the units, as it allows for easier comparison with values found in the literature.

Parameter	Description	Value	Unit
$\beta_{p,\,Pliocene}$	Representative vertical compressibility Pliocene deposits	1e−8	m^2/N
$\beta_{p,\,Miocene}$	Representative vertical compressibility Miocene deposits	7.5e−9	m^2/N
$\beta_{p,\,Evaporites}$	Representative vertical compressibility evaporites	1e−10	m^2/N
$\rho_b - \rho_w$	Bulk density minus density fresh water	1100	kg/m^3
$\frac{\partial z_b}{\partial t}$	Sedimentation rate	3.9e−4–2.7e−4	m/year
$n_{Pliocene}$	Representative effective porosity Pliocene deposits	0.10	–
$n_{Miocene}$	Representative effective porosity Miocene deposits	0.10	–
$n_{Evaporites}$	Representative effective porosity evaporites	0.01	–
$\frac{\partial \rho}{\partial C}$	Slope linear equation of state	0.71	$(kg/m^3)/(g/l)$
$K_{v,\,Pliocene}$	Vertical hydraulic conductivity Pliocene	1e−4	m/d
$K_{v,\,Miocene}$	Vertical hydraulic conductivity Miocene	1	m/d
$K_{v,\,Evaporites}$	Vertical hydraulic conductivity evaporites	1e−8	m/d
α_l, α_t, α_v	Longitudinal, transversal and vertical dispersion length	10, 1, 0.1	m
D_c^*	Effective molecular diffusion	22.9e−10	m^2/s

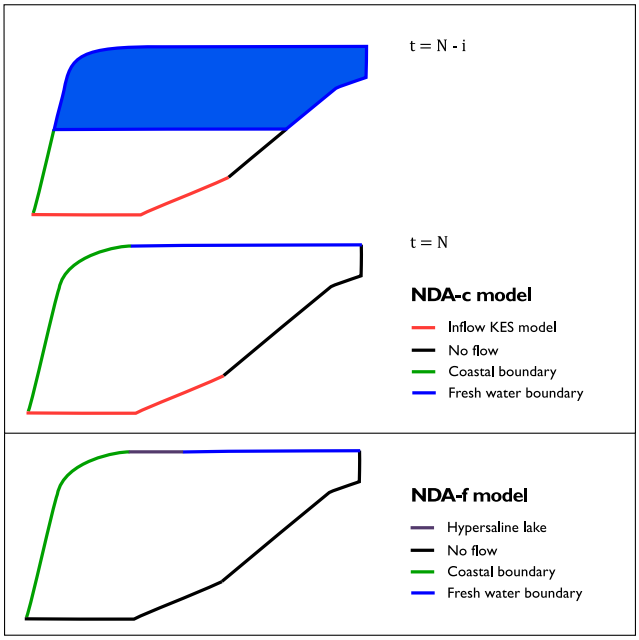

Fig. 2. Boundary condition types for the NDA models. The NDA-c model figure shows 2 plots, the bottom plot is at the end of the time domain (t = N), the upper a moment in the time domain (t = N-i).

increases, the conductance of the top boundary of the KES model (m^2/d) was adapted. SEAWAT takes the conductance as input for its Cauchy boundary condition, together with a prescribed head. The conductance is defined as follows (Guo and Langevin, 2002):

$$Cond = \frac{KA}{l} \tag{17}$$

where K is the hydraulic conductivity, A is the cross-sectional area of the flow, l is the distance of the boundary to the model cell (m). We increased this conductance with time as sedimentation progresses:

$$Cond = \frac{K_{v,\,sand} A_{cell\ top}}{\frac{\partial z_b}{\partial t} t} \tag{18}$$

$K_{v,\,sand}$ is the vertical hydraulic conductivity of the NDA deposits (m/d), $A_{cell\ top}$ is the area of a model cell top interface (m^2), t is the time (d), and $\frac{\partial z_b}{\partial t}$ is the sedimentation rate (m/d). All other boundaries were assumed to be no flow boundaries.

As for the initial conditions, we assumed completely stagnant conditions during the Pliocene, and therefore applied 3.4 million years (duration of the Pliocene) of molecular diffusion over the KES clay layer. The initial TDS concentration at the Miocene deposits varied between 125, 200, 300, 400 g/l, (respectively scenarios M125, M200, M300, and M400), and the initial groundwater age of the Miocene deposits was set at 3.4 million years. The upward salt fluxes of the KES scenario that showed the best fit to pressure observations were injected into the NDA-c model, as part of a "base case". In this base case, all parameters of the NDA-c model were set in favor of hypothesis 3, based on their expected behavior.

4.3.2.2. NDA models. The boundary conditions of both NDA models are shown in Fig. 2. The fresh water boundary had a fixed point water head, linearly increasing land inwards, roughly following the topography of the delta. The coastal boundary of the NDA models was modeled either open or closed off from 250 m to 1000 m depth (see also Section 4.3.2.3), as the connectivity between the deeper parts of the NDA and the sea is still uncertain. The geometry of this boundary was determined with the General Bathymetric Chart for the Oceans' gridded dataset (GEBCO, 2014). This is a 30 arc-second grid, providing global bathymetric coverage. In addition, four horizontal clay layers were placed at different depths, spanning from the coastal boundary to the middle of the onshore model domain, following the conceptual cross-section by Shata and Hefny (1995).

At the bottom of the NDA-c model, the model receives its flow, dissolved salts and groundwater ages from the KES model as a fixed flux. The large time domain of the NDA-c model (2.5e6 years) matches the extent of the deposition of sediments that form the NDA. Therefore, the aquifer is initially thin at the start of the Pleistocene and grows in thickness with time; this implies that the distance between the bottom and top boundary increases with time. SEAWAT does not support a change of spatial domain size over time, therefore we ensured the "undeposited" part of the model did not contribute to the flow or solute transport system by making every "undeposited" cell a Cauchy boundary cell with zero salinity and a head matching the sea level at that timestep. After "deposition" of a cell, the boundary condition in that cell was deactivated, turning it into a regular active cell. This created stacked Cauchy boundaries (Fig. 2), which were deactivated upwards as sedimentation progresses. The validity of this approach is shown in Appendix C. We used the most parsimonious sedimentation possible, namely assuming a constant sedimentation rate. With this we determined the location of the Cauchy boundary cells apriori for every input timestep (called "stress-period" in SEAWAT). We used a number of input timesteps (365) that exceeded the amount of model layers (100), to ensure the most gradual increase of the aquifer size that was possible.

On top of the NDA-f model, a hypothetical 50 km long hypersaline inundation of 90 g/l was added for 8000 years, roughly the spatiotemporal extent of the Late Pleistocene Sabkha muds near the current coastline (Stanley and Warne, 1993), as these were the most favorable circumstances for free convection (Appendix B). It is assumed that free convection was not limited by salt production or by water availability. The aim of the free convection model was not to accurately model chaotic fingering patterns nor

their onset, as these are controlled by a) model discretization (for example, see Kooi et al., 2000; Prasad and Simmons, 2005; Zimmermann et al., 2006); b) heterogeneity (Simmons et al., 2001; Post and Simmons, 2010); c) dimensionality (Simmons et al., 2010); d) numerical solvers chosen (Zimmermann et al., 2006); e) dynamic boundary conditions, e.g. as reflected by the differences between the dimensionless numbers in Nield (1968) and Wooding et al. (1997) for flooded and dry circumstances respectively. This model was intended to obtain a sense of the time scale of free convection in a regional groundwater system of this size, for which this setup is sufficient (Fig. D2). For this model, a warm-up period of 120,000 years was chosen to set the initial conditions, roughly the extent of a glaciation cycle, but sea levels were kept constant to their relatively high current level, for the sake of parsimony. To ensure both vertical and horizontal propagation of hypersaline plumes, the clay layers were further extended land-inward with a conductivity of:

$$\log(K_{extension}) = \frac{\log(K_{sand}) + \log(K_{clay})}{2} \tag{19}$$

Without this extension, hypersaline plumes would only travel vertically downwards without intruding horizontally in-between clay layers. The conceptual idea behind this extension is a clay layer becoming thinner land-inwards (see also Fig. 1b), thus reducing in hydraulic conductivity.

4.3.2.3. Sensitivity analysis. A sensitivity analysis was performed on the compaction models (KES+NDA-c), to study the influence of some of the underlying assumptions on the results. Inputs (parameters, boundary conditions and initial conditions) were altered one at a time from a base case, of which the values can be found in Table 3. Firstly, the initial concentration in the Miocene deposits in KES was increased from 125 g/l to 200 g/l and the increased upward salt flux is injected into NDA-c model. Secondly, the horizontal clay layers in the NDA-c model were removed. Thirdly, the river stage at the apex was increased from 5 m to 15 m. Fourthly, the hydraulic conductivity of the NDA-c model was increased from 10 m/d to 25 m/d and 75 m/d, respectively. Finally, the bottom 750 m of the seaside boundary was either open or closed off, by setting the conductance (Eq. (17)) of the sea boundary to 1000 m^2/d or 2.5e−9 m^2/d. The first is seen as an extreme upper limit, and was calculated by assuming a 1 m thick layer of gravel of 100 m/d, and multiplying this by the area of a horizontal cell interface (10 m^2). The latter was calculated by multiplying an assumed horizontal hydraulic conductivity for unweathered marine clay (5e−6 m/d) by the area of a horizontal cell interface (10 m^2) and dividing this by the maximum observed horizontal extent of 20 km (Abdel Aal et al., 2000), and thus presents a lower limit. Scenarios were compared by looking at the depth difference between the 70 g/l isoconcentration line and 600 m at three observation locations, ε (m).

Table 3
Parameters for the NDA-c model. In brackets the parameter value alterations for the NDA-f model. We are purposely inconsistent with units, as it allows for easier comparison with values found in the literature.

Parameter	Description	Value	Unit
$K_{h,sand}$	Horizontal hydraulic conductivity sand. Compaction case and free convection case	10 [75]	m/d
$K_{h,clay}$	Horizontal hydraulic conductivity horizontal clay layer.	5e−4	m/d
$\frac{K_h}{K_v}$	Anisotropy	10	–
α_l, α_t, α_v	Longitudinal, transversal and vertical dispersion length	10, 1, 0.1	m
n_e	Effective porosity	0.10	–
$\frac{\partial z_b}{\partial t}$	Sedimentation rate	3.9e−4 [0]	m/year
$\frac{\Delta h_{riv}}{\Delta x}$	River gradient	3.125e−2 [9.375e−2]	m/km
S_f	Specific storage in terms of fresh water head	1e−5	1/m
$\frac{\partial \rho}{\partial C}$	Slope linear equation of state	0.71	(kg/m^3)/(g/l)

5. Results

5.1. Hypothesis 1: Molecular diffusion

Fig. 3 shows that, even given a TDS concentration of 643 g/l, the highest ever measured as far as we are aware of (Hanor, 1994), the concentration at 1000 m depth is still below the observed concentration at 600 m depth. Even though all parameters are set in favor of this hypothesis, the observed TDS cannot be reproduced, which means that diffusion cannot be the sole cause of the observed hypersalinity at 600 m and there has to be at least a second process involved to cause enough upward salt transport through KES.

5.2. Hypothesis 2: Double diffusiveconvection

Filling in the most favorable limits for this hypothesis (see Table 1 for their values) results in $Ra_t + Ra_c$ being strongly negative (−516), which is caused by the high Le (690). This entails that the buoyancy due to salinity works very stabilizing. Assuming there is enough mechanical dispersion (D_{mch}) so that the theoretical minimum of Le is approached:

$$\lim_{D_{mch}\to+\infty} Le = \lim_{D_{mch}\to+\infty} \frac{D_t + D_{mch}}{D_c^* + D_{mch}} = 1 \tag{20}$$

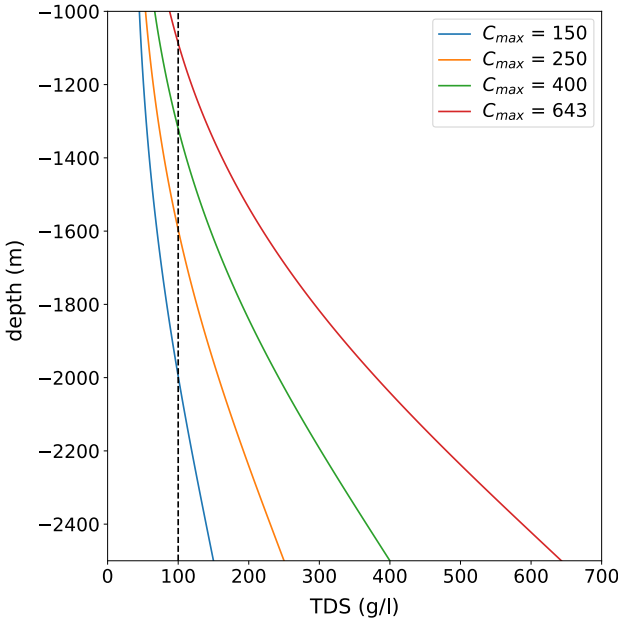

Fig. 3. Modeled concentrations of pure molecular diffusion with depth for different maximum concentrations over the KES formation after 5.33 million years (from the start of the Pliocene to present). The dashed line presents the maximum measured concentration that was measured at 600 m depth (100 g/l).

Then, given the parameters in Table 1, still $N \approx -1$, meaning that:

$$Ra_t + Ra_c = Ra_t + Ra_t NLe \approx Ra_t - Ra_t \approx 0 \quad (21)$$

Furthermore, $Ra_t = 0.089 \ll Ra_{crit}$. So even with a constant salinity gradient, no free thermohaline convection is expected. Based on the high Le, $N \approx -1$, and low Ra_t, it is unlikely that there was any upward transport of solutes due to thermohaline induced free convection through KES. The thick, low-permeable KES formation's potential for dampening instabilities is too high for any large-scale instability to occur.

5.3. Hypothesis 3: Sediment compaction

Fig. 4a shows a comparison between modeled pressures and observations in a well near the city of Kafr El Sheikh [personal communication with dr. M. Tingay], per initial concentration scenario M125-M400. Both observations and our models follow a hydrostatic pressure distribution up to a depth of less than approximately 2.8 km, to which an initial concentration of 125 g/l seems to give the best fit. Around 2.8 km depth the observations show a sudden jump in pressure, indicating the presence of a low permeable seal, which consists of the Messinian evaporites (Rizzini et al., 1978; Nashaat, 1998). This seal is not completely impermeable; otherwise the observed pressure underneath the seal would approach lithostatic pressure. Our models also capture the pressure difference across this Messinian seal, which means that the upward groundwater flow encounters enough resistance. The resistance in our model might be overestimated as part of the pressure difference may already have been established during the Pliocene. In addition, the dissolved salts had more time to be transported through the seal. Thus our model represents a conservative estimate of upward salt transport. Fig. 4b shows hypersaline groundwater with a concentration above the observed 100 g/l (Fig. 1a) moving from the KES to the NDA due to compaction-induced upward salt transport and molecular diffusion. The increasing concentrations over time imply that salt transport has not yet reached steady state. Therefore, if the hypersaline groundwater in the NDA is caused by compaction-induced salt transport, the mass flux of salt into the NDA is still present and presumably even increasing slowly on a geological time scale.

The results in Fig. 5a as obtained from the NDA-c model show that these upward salt mass fluxes from the KES to the NDA have the potential to cause salinities similar to those observed at 600 m depth in the NDA nowadays. Furthermore, if this has indeed occurred in reality, the hypersaline groundwater should be older than 2.5 million years, and thus older than its surrounding sediment matrix. A subsequent sensitivity analysis shows that hypothesis 3 only holds if the bottom of the coastal boundary is closed as shown in Fig. 5b. If the boundary were open, the TDS at 600 m would decrease towards the coast (see also Fig. A1), which is not observed in the field (Fig. 1a). Moreover, with an open coastal boundary, the 70 g/l contour would not reach 600 m.

5.4. Hypothesis 4: Free convection

In the NDA-f model, a considerable volume of hypersaline groundwater is transported downwards in this model (Fig. 6). After onset, the plume travels downwards for roughly 600 years until it reaches the bottom. This plume subsequently reaches the observation points in the case of an open boundary, but does not in the case of closed boundary. A closed coastal boundary in our model results in rejection of the NDA-f hypothesis: the hypersaline groundwater has difficulty to replace fresh groundwater that is trapped between clay layers and a closed coastal boundary.

We also make two observations that might be relevant to groundwater age measurement campaigns in the future. Firstly, free convective transport leads to an inversion in groundwater ages (Fig. 6 left), though this inversion becomes negligible on longer timescales with an open coastal boundary (Fig. 6 right, see also Supplementary Video A2). Secondly, it is observed that a closed boundary results in groundwater ages exceeding the duration of glacial cycles (100,000 year, see also Supplementary Video A3),

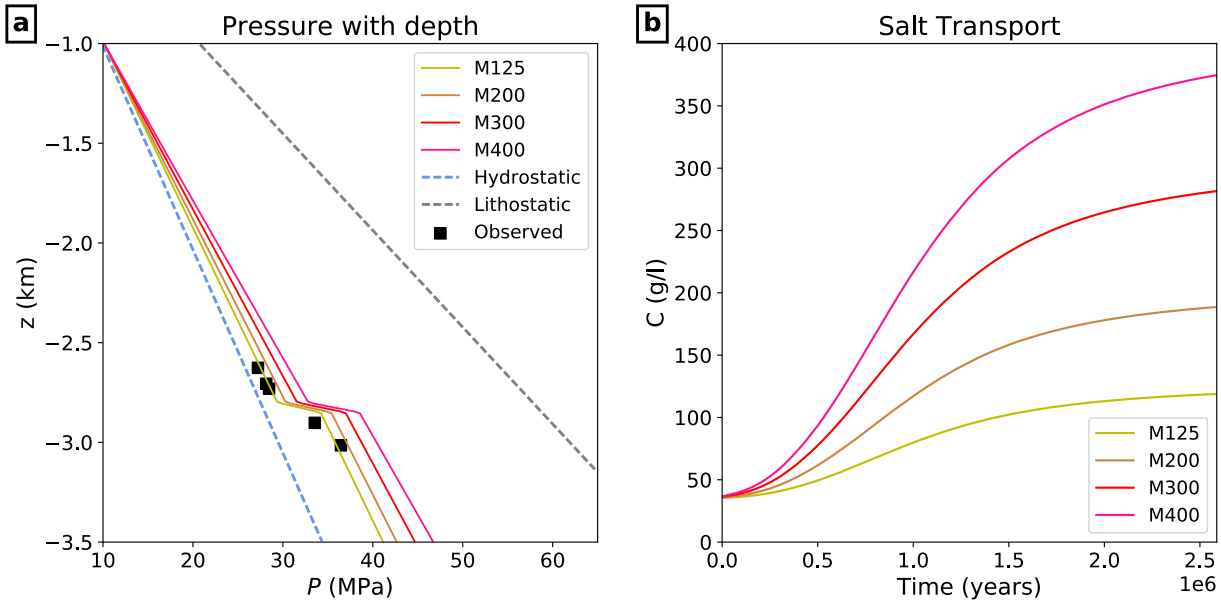

Fig. 4. (a) Modeled pressure with depth, varied over different initial concentrations. M125–M400 represent the KES model results, where the number indicates the initial concentration taken for the Miocene deposits. The hydrostatic pressure is calculated with a density of fresh water (1000 kg/m^3) and represents the minimum expected pressure. The lithostatic pressure is calculated with a ρ_b of 2100 kg/m^3 and represents the maximum possible pressure. The observations are from a well near the city of Kafr El Sheikh. (b) Concentrations (C) at x = 0 across the top boundary of the KES model.

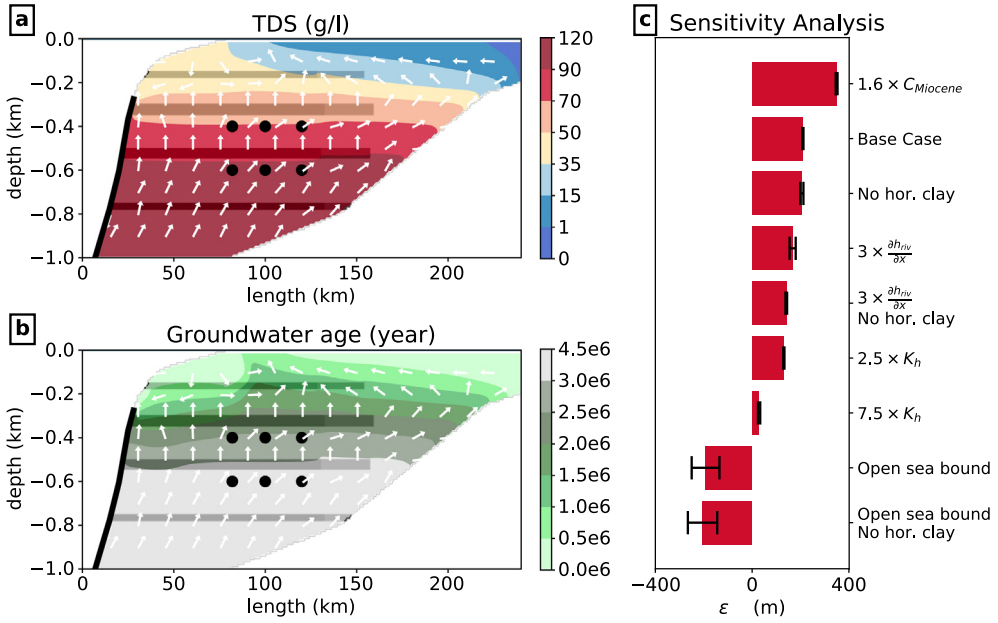

Fig. 5. (a and b) Salinities (TDS) and groundwater ages after 2.5 million years in the base case NDA-c model. The black dots represent the approximate location where observations are taken; the white arrows indicate the direction of the groundwater flow; the shaded areas represent the location of clay layers in the model. Note that the cross-section is stretched in the vertical direction by a factor 100. The left upper intrusion of young groundwater is caused by the sudden shift land inwards of the coastal boundary when the sea level rises over the top left rounded corner of the delta front. (c) Bar plot showing the results of a sensitivity analysis performed with the NDA-c model. ε is the depth difference between the observation locations (3 points at 600 m depth) and the 70 g/l isoconcentration contour at the observation locations. The error bars show the range of ε; a higher range means a stronger inclined isoconcentration line. For input values, see Table 3.

despite the high hydraulic conductivity (75 m/d) and low porosity (0.10) of the aquifer in this model.

6. Discussion

Our computational investigation did not lead to a final conclusion as to the origins of the hypersaline groundwater. Consequently a brief discussion of measurements to discriminate hypothesis 3 from 4 is necessary. With groundwater dating it might be possible to discriminate these two hypotheses. Upward compaction-induced salt transport leads to groundwater ages older than the surrounding sediment matrix. Since overpressures are a common phenomenon in deltas (Sharp and Domenico, 1976; Neuzil, 2003), it is safe to assume that the same holds for upward transport of major volumes of connate groundwater into delta aquifers, e.g. as presumably occurred in The Netherlands (Verweij, 1999; Griffioen et al., 2016). Whether this groundwater is still present in these aquifers highly depends on the hydrogeological connection between aquifer and sea. This connection is critical to coastal hydrogeology (Yechieli et al., 2009), since it also influences potential offshore fresh water reserves (Post et al., 2013) and submarine groundwater discharge (Taniguchi et al., 2002). Groundwater dating in combination with our current analysis could thus lead to important conclusions regarding both the origins of the hypersaline groundwater and the interaction between the deeper parts of the NDA and the Mediterranean Sea. If the groundwater is found to be older than 2 million years old (Fig. 5), it originates from Messinian deposits and the hydrogeological connection with the sea is limited. In contrast, if it is found to be younger than 100,000 years old, it presumably is the result of free convective systems and the coastal boundary is open. ^{81}Kr-dating may be the most suitable method to discriminate these two hypotheses (Sturchio et al., 2004; Aeschbach-Hertig, 2014), as ^{36}Cl-dating is not suited for saline fluids (Park et al., 2002).

Determining the chemical composition of the groundwater and comparing this to published cases will certainly lead to new insights. A start would be the Br^-/Cl^- ratio, which is useful in discriminating whether salinity is caused by evapoconcentration or rock salt dissolution (Hanor, 1994). This is not necessarily enough information to discriminate hypothesis 3 from 4, since the groundwater from underneath the KES could also have been evapoconcentrated during the Messinian, as thought to have happened in the East Mediterranean Sea (Vengosh et al., 1998). More suitable might be non-conservative environmental tracers that interact with clay, as hypersaline groundwater of hypothesis 3 had more time to interact with clay minerals, under higher temperatures, than groundwater of hypothesis 4. Examples of these are Na^+, Ca^{2+}, Sr^{2+}, B, K^+, and δ^{11} B (Vengosh et al., 1999). Useful cases for the comparison are the hypersaline water found in the deep eastern Mediterranean basin (Vengosh et al., 1998) and at the coastal sabkhas in the Northern Sinai (Levy, 1977; Gat and Levy, 1978), which might be suitable analogues for the hypersaline groundwater of respectively hypothesis 3 and 4.

There are limitations to this computational investigation. Regarding the free convection model (NDA-f), it is difficult to constrain a paleo-reconstruction of a process controlled so strongly by heterogeneity and that acted on such a relatively small timescale. This is in part reflected by the very limited number of field observations of free convection in groundwater; despite over a century of research, the first field observations started to be reported only in the last decade (Andersen et al., 2007; Van Dam et al., 2009). In addition, our assumption of free convection unrestricted by salt or fluid availability is applicable to a sabkha delta which continuously receives new saline water, but may be inappropriate for a floodplain. Furthermore, in both this model and NDA-c we did not take the sea level variation of a glacial cycle into account. The low sea-level stands during a glacial period would result in a wider fresh water zone (Post et al., 2013) and the sea level variations might also result in a wider mixing zone, e.g. as happens on a larger spatiotemporal scale in carbonate platforms (Jones et al., 2002). The effect of a higher hydraulic gradient on the NDA-c model is shown in the sensitivity analysis, though not to the extent as the gradient

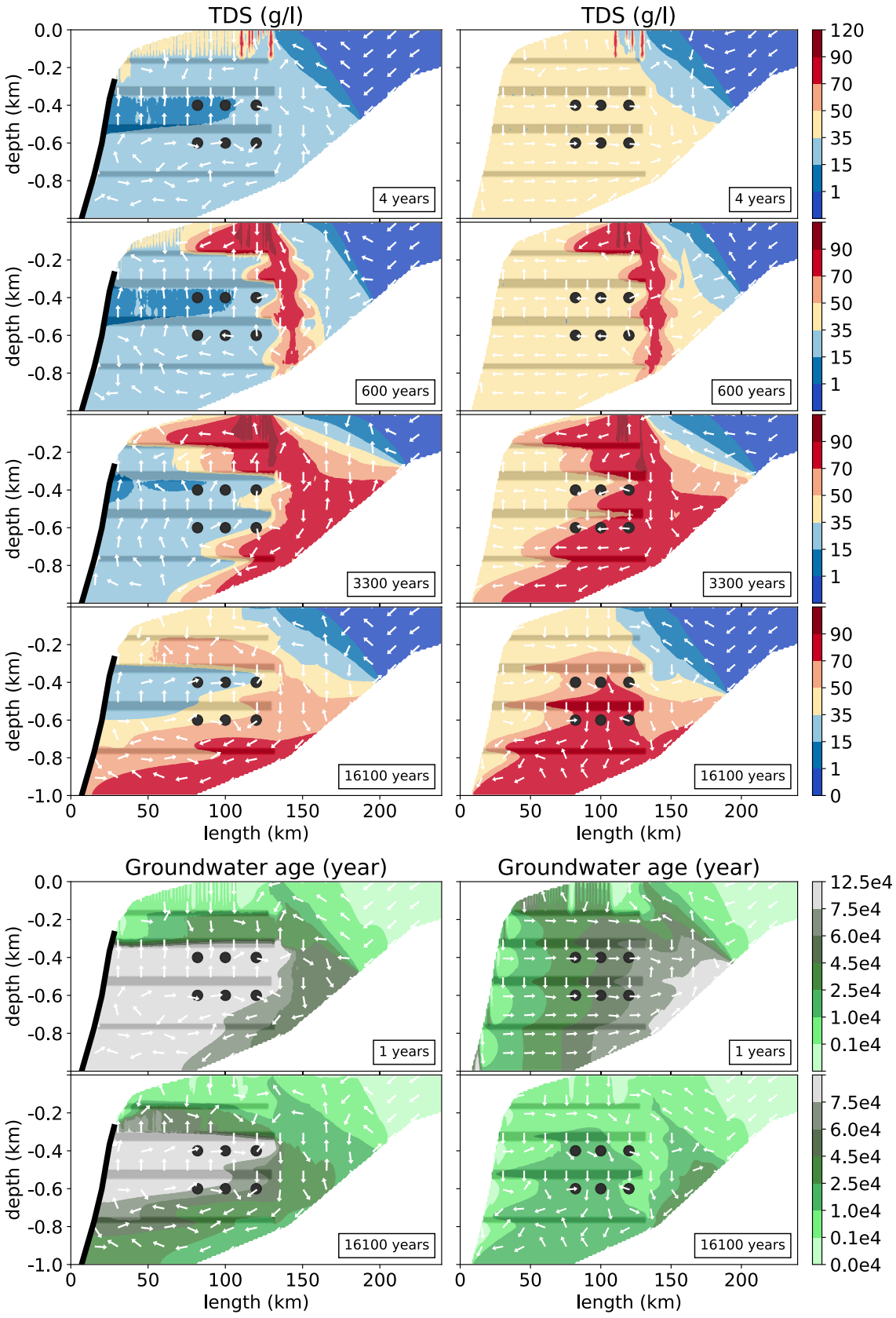

Fig. 6. Salinities and groundwater ages after a hypersaline inundation (of c = 90 g/l, that lasted 8000 years) was formed. Note that the NDA-f model had 120,000 years of spin-up time prior to the inundation (reflected in the groundwater ages) and that the groundwater ages legend scale differs from that in Fig. 5a. The left hand column presents the results with a closed off coastal boundary, the right with an open boundary. The ribbed shape of the downward moving plume at 600 years is due to the horizontal extensions of the clay layers, see Eq. (19).

reached during the Pleistocene. In short, our results intentionally present a hypothetical, extreme case.

Regarding the KES model, it is possible that the hydrogeological system in the pre-Miocene deposits is connected to the Miocene deposits in some compartimized areas through faults, which may imply that thermal processes become important in determining the salt concentration underneath the KES formation (Garven, 1995; Lopez and Smith, 1995). However, this is excluded from this research, because of the scarcity of published data of the deep hydrogeology underneath the Nile Delta. Furthermore, we assumed that the side boundaries are impermeable due to faulting. For the side boundary offshore (in the north) this is reasonable, given the high lateral differences in overpressure (Nashaat, 1998), but onshore this might be different. As far as we are aware off, no pressure measurements in the deeper strata underneath the Nile Valley have been published to assess the validity of this assumption.

Two processes are not covered in this research, which could serve as alternative hypotheses. Firstly, hypersaline groundwater may preferentially flow along faults, as faults are observed that propagate through the KES formation (Abd-Allah et al., 2012). These faults might act as a conduit for upward flow (Bense et al., 2013). Secondly, leaking abandoned petroleum exploration wells could act as an anthropogenic source of salt water. At least 90 wells had been drilled in 1989 (Sestini, 1989) because of the area's high oil and natural gas potential (Kirschbaum et al., 2010), which may potentially leak hypersaline groundwater upwards driven by the overpressures underneath KES. This would result in high salinities focused around exploration areas. Both these processes would result in a more heterogeneous distribution of salinities and also in temperature anomalies (Bense et al., 2013), thus testing these two hypotheses requires more data than is currently available and is therefore a topic for further research.

The origins of the hypersaline groundwater have crucial implications for the expected occurrence of deeper fresh water pockets; our results show that the salinity distribution by free convection is largely affected by clay layers whereas the slow compaction-induced upward advection is quite insensitive to these layers. Our models with free convection show that lower salinity water might be trapped between clay layers, whereas no salinity inversions were simulated in models with sedimentation compaction as the driver.

7. Conclusions

Two of the four hypotheses of this research remain valid. The hypersaline groundwater in the NDA is either caused by compaction-induced salt transport (hypothesis 3) or free convective systems (hypothesis 4). Both the NDA-c model and the NDA-f model are able to reproduce the observed high TDS values, given the right coastal boundary condition. This condition has opposite effects on the plausibility of these models; an open boundary results in the rejection of the NDA-c model (the hypersaline groundwater does not reach 600 m depth), whereas in the NDA-f model a closed boundary hinders the hypersaline groundwater in replacing the fresh water between the clay layers, and in our conceptualization, reaching the observation point.

The origins of this hypersaline groundwater affect the probability of the existence of deep fresh water pockets. This probability is reduced if the hypersaline groundwater originates from underneath the KES and was transported upwards following the assumptions made in this paper. Deep fresh water pockets are considered more probable if the hypersaline groundwater was brought downwards by free convection.

Acknowledgements

Firstly, we thank Hanneke Verweij and Andrea Forzoni for their helpful ideas and remarks on the hydrogeology. Secondly, we thank Mark Tingay for kindly providing us with overpressure data. Thirdly, we thank two anonymous reviewers for their critical, helpful comments and remarks, which greatly enhanced the quality of this paper. This research is financially supported by the Netherlands Organization for Scientific Research (NWO), and carried out within The New Delta program. The data used are listed in the references and supplements.

Appendix A. Supplementary results

See Fig. A1.

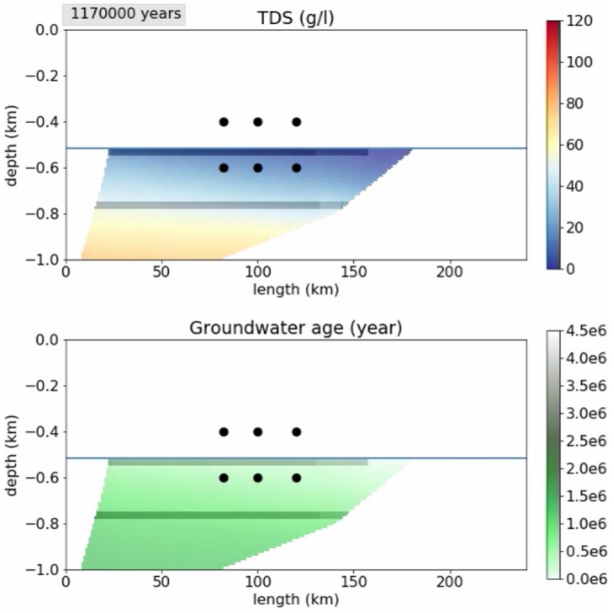

Video A1. Animation of the results of the NDA-c model, for the Base Case simulation. The upward blue line represents the current sedimentation level.

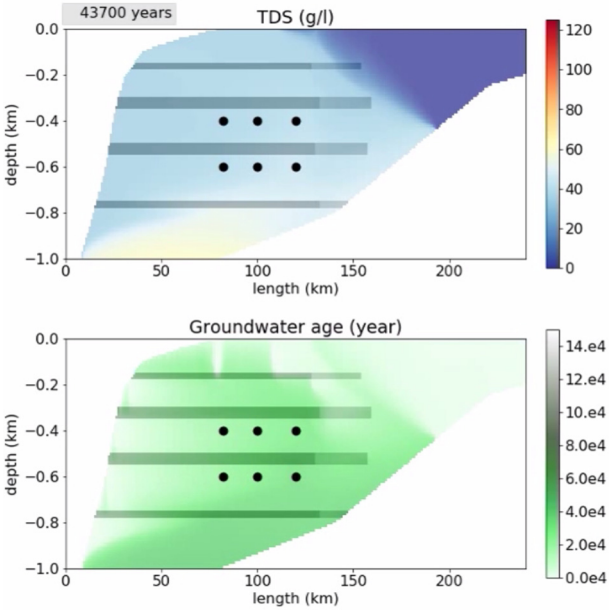

Video A2. Animation of the results of the NDA-f model with an open sea boundary.

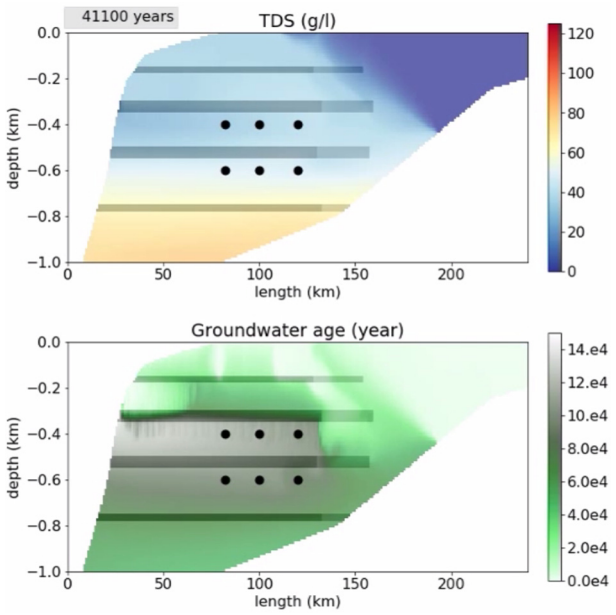

Video A3. Animation of the results of the NDA-f model with a closed sea boundary.

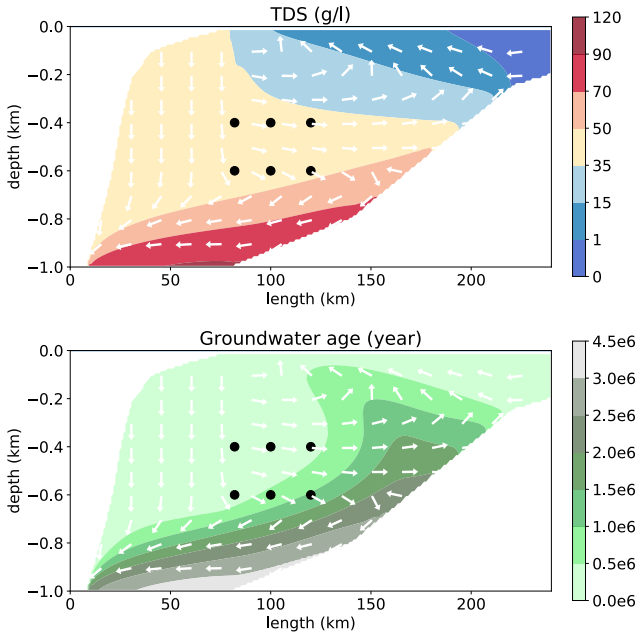

Fig. A1. Salinities (TDS) and groundwater ages after 2.5 million years in the open case NDA-c model without clay layers. The black dots represent the approximate location where observations are taken; the white arrows indicate the direction of the groundwater flow. Note that the cross-section is stretched in the vertical direction by a factor 100.

Appendix B. Onset of convection during the Pleistocene and Holocene

We assess the onset of free convection under two conditions applicable to (semi-)arid deltas: during an inundation and during a dry stand. For values, sources and definitions of symbols used in this analysis, the reader is referred to Table B1. The onset of free convection underneath a dry salt lake is determined by the destabilizing buoyancy force and the stabilizing upward flux caused by evapotranspiration (Zimmermann et al., 2006). Wooding et al. (1997) derived a dimensionless number for the (theoretical) onset of free convection underneath a dry salt lake, with impermeable boundaries at the bottom and sides:

$$R_\delta = \frac{(\rho_m - \rho_a)K_v n_e}{\rho_a ET} \tag{B.1}$$

where ρ_m and ρ_a are the salinity of the salt lake and surrounding water (kg/m^3), respectively, K_v is the vertical hydraulic conductivity (m/d), n_e is the effective porosity (−), and ET the evapotranspiration rate (m/d). It was found, with both lab and numerical experiments, that for R_δ values above 10, free convection is expected (Wooding et al., 1997). For flooded conditions the onset of free convection can be assessed by the Rayleigh number (Nield and Bejan, 2013):

$$Ra_c = \frac{(\rho_m - \rho_a)K_v H}{\rho_a D} \tag{B.2}$$

where H is the thickness of the aquifer (m). And D is the dispersion tensor (m^2/d), here taken as the scalar effective diffusion constant D_c^* (since we assume initially stagnant water). With a fixed head on top (due to an inundation), the critical value for $Ra_c = 27.10$ (Nield, 1968). Important underlying assumptions of both these dimensionless numbers are a) a homogeneous hydraulic conductivity, b) a linear upward trend in concentration, and c) initially stagnant water. We, therefore, want to stress that the values of these numbers only allow for a qualitative interpretation, as, under field conditions, free convection can still occur below these critical numbers due to heterogeneities, non-linear trends in concentration and changing boundary conditions (Simmons et al., 2001).

For $K_v = K_{v,clay}$, $R_\delta = 0.19$ and $Ra_c = 3600$; and for $K_v = K_{v,sand}$, $R_\delta = 470$ and $Ra_c = 8.6e7$. We interpret these values as follows: during the Pleistocene, amidst a salt inversion, free convection endured little resistance and definitely developed. During the Holocene, buoyancy forces endured increasing resistance from the deposited clay. Free convection likely still occurred with inundations during and after dry periods, where respectively evapoconcentration and dissolution of salts might have occurred, but unlikely occurred on a large scale during periods without any inundations.

Table B1
Limits of parameters chosen in Rayleigh and Wooding number analysis (Eqs. (1) and (2)). We are purposely inconsistent with units as this allows for better comparison with the literature.

Symbol	Description	Value range	Unit	Source
n_e	Effective porosity	0.05–0.45	–	Helalia (1993)
$K_{v,clay}$	Vertical conductivity Holocene clay	0.001–0.01	m/d	Laeven (1991)
$K_{v,sand}$	Vertical conductivity Pleistocene sand	3.6–24.0	m/d	Sefelnasr and Sherif (2014)
$\frac{\rho_m-\rho_a}{\rho_a}$	Relative density	0.071	–	Assumed
ET	Evapotranspiration flux	600–1100	mm/yr	Stanley and Jorstad (2006)
D_c^*	Effective molecular diffusion	22.9e−10	m^2/s	See Section 4.1
H	Vertical length scale, taken as aquifer thickness	1000	m	Farid (1980)

Appendix C: A comparison between compaction in SEAWAT and an analytical solution

Here, we compare numerical results of overpressure to the analytical solution of Bredehoeft and Hanshaw (1968), who wrote the original solution of Gibson (1958) in terms of excess head instead of excess pressure. They define excess head as:

$$h' = h - h_s \tag{C.1}$$

where h is head, h_s is the steady state component of head if there would be no compaction, and h' is the excess head generated by compaction. The latter component can be transient. Assuming a constant density of incompressible water and homogeneous hydraulic conductivity and by ignoring compression in the spatial derivatives, the one dimensional equation that describes the excess head in sediments is:

$$K\frac{\partial^2 h'}{\partial z^2} = S_s\left[\frac{\partial h\prime}{\partial t} - \frac{\rho'}{\rho_w}\frac{\partial l}{\partial t}\right] \tag{C.2}$$

With:

$$\rho' = \rho_b - \rho_w \tag{C.3}$$

where K is the hydraulic conductivity, z is the height above the impermeable base, S_s is the specific storage, t is time, ρ_b is the bulk density of the sediments, ρ_w is the density of fresh water, and l is the sediment thickness. Gibson considered the following problem: sediment is deposited at a constant rate on top of an impermeable base. This base is taken as the reference datum. The sediment deposition causes the upward boundary, where $h\prime = 0$, to move upwards at constant rate. The initial thickness of the aquifer is zero. The equation that describes excess head with time and depth is then:

$$h' = \frac{l\rho'}{\rho_w} - \frac{l\rho'}{\rho_w}\left(\frac{\pi Kt}{S_s l^2}\right)^{-\frac{1}{2}} \exp\left[-\left(\frac{z}{l}\right)^2 \frac{S_s l^2}{4Kt}\right] \cdot \int_0^\infty \xi' \tanh\left(\frac{\xi' S_s l^2}{2Kt}\right) \cosh\left[\left(\frac{z}{l}\right)\frac{\xi' S_s l^2}{2Kt}\right] \exp\left(-\frac{\xi'^2 S_s l^2}{4Kt}\right) \mathrm{d}\xi' \tag{C.4}$$

For a derivation see Bredehoeft and Hanshaw (1968) and Gibson (1958). If we assume $h_s = 0$, then $h' = h$ and we can calculate the amount of overpressure generated with SEAWAT. This requires two boundary conditions to be set in SEAWAT: An upward moving top boundary and a volumetric source term, which equals the strain rate. The first is implemented similar as how we approached the Pleistocene sedimentation in the NDA-c model: By stacking Cauchy boundary cells and deactivating them upwards through time. The latter is implemented as how we modeled the effects of compaction on groundwater flow in the KES model, by adding source terms to every cell in the domain injecting a fixed flux, equalling the strain rate, in this case:

$$q_s = S_s\left[\frac{\rho'}{\rho_w}\frac{\partial l}{\partial t}\right] \tag{C.5}$$

Eq. (C.5) is very similar to Eq. (15) in the main text. For the reader familiar with SEAWAT, we used the GHB and the WEL package respectively.

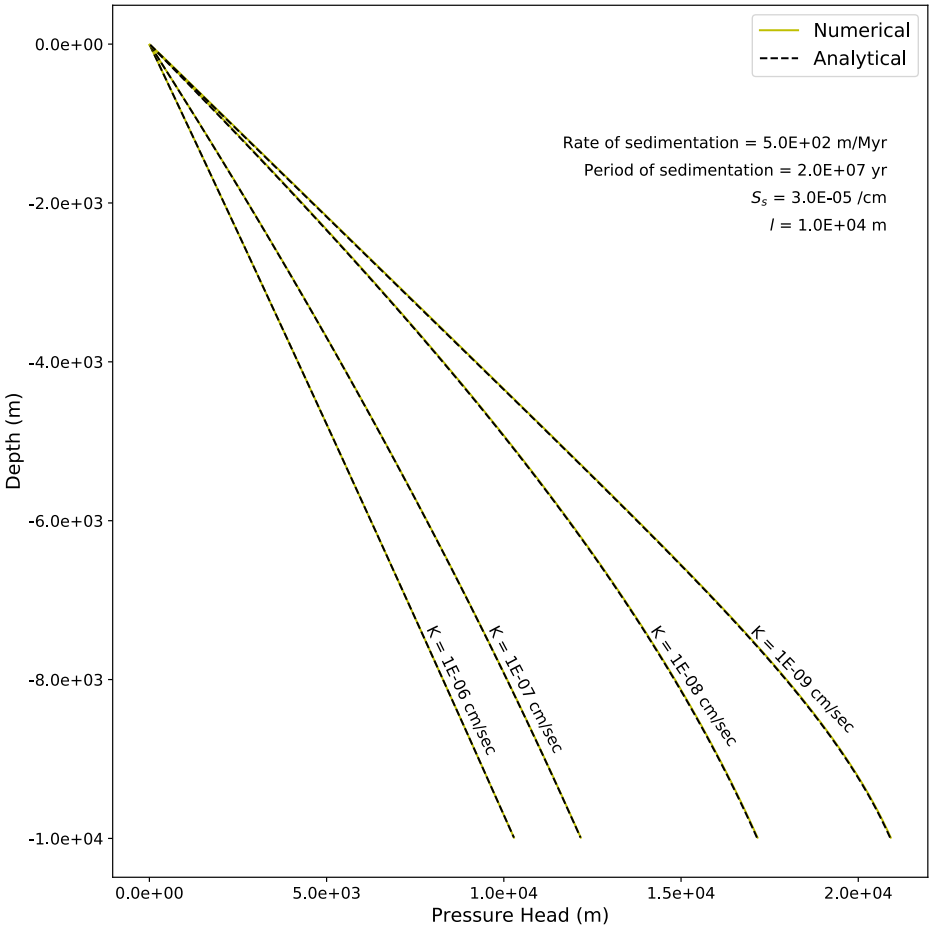

Fig. C1. Recreation of Fig. 6 in Bredehoeft and Hanshaw (1968), including our numerical results, showing an excellent fit.

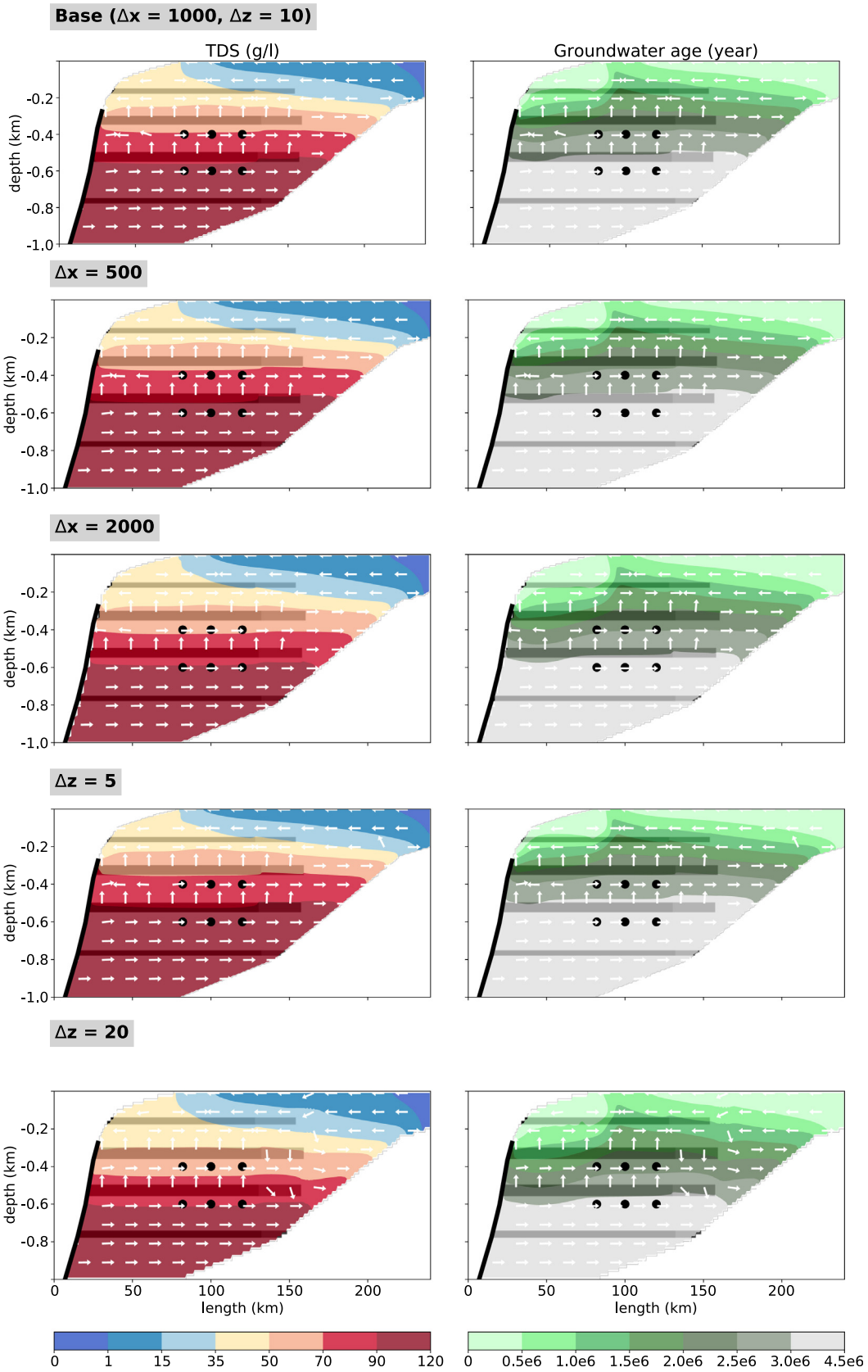

Fig. D1. Grid convergence test of the NDA-c model. The white arrows now represent velocities instead of fluxes, as in Fig. 3. The grey box shows the grid cell size deviations from the base case.

In Fig. C1 we recreated Fig. 6 in Bredehoeft and Hanshaw (1968). It shows an excellent fit between the numerical model and analytical solution. We conclude that using SEAWAT in combination with our modifications is appropriate to model groundwater problems on a geological timescale, as one can solve a moving boundary problem and incorporate the effects of compaction with SEAWAT.

Appendix D: Effects of cell discretization

A grid convergence test was conducted for both the KES model as the NDA-c model. Cell discretization was decreased or increased in both dimensions, one at a time. As the KES model provides the basal boundary condition for the NDA-c model, we ensured that the models had the same cell size in each simulation. Thus hypothetical numerical errors of the KES model are also reflected in the TDS distribution of the NDA-c model. Fig. D1 shows a comparison of the TDS contours of the NDA-c model. The contours for the finer discretization are sufficiently similar to the base case. The coarser grid sizes tend to underestimate the height of the 70 g/l contour; we ascribe this to numerical dispersion. We conclude that the cell size is sufficient and if it were not, it would not affect our conclusions in this paper, since the 70 g/l contour would only be higher.

For the NDA-f model, a different approach was taken, to assess the effect of a wider range of Δx, since this dimension had the coarsest resolution (1 km). We modeled a simple 800 m thick sandbox with a hypersaline lake on top. This allowed us to stretch the domain as much as necessary in the horizontal direction. The chosen parameters for this model are the same as in Table 3. The amount of cells was kept at 100 in the horizontal direction. Ξ is the normalized fluid mass increase, which is calculated by dividing the increase in fluid mass across the top boundary by the maximum mass storage increase:

$$\Xi = \frac{\int\int \frac{Q}{\Delta x}\rho \mathrm{d}x\mathrm{d}t}{V_{tot}\left((\rho_{max}-\rho_0)n+\frac{1}{2}S_f\frac{\rho_{max}-\rho_0}{\rho_0}z_{max}\rho_{max}\right)} \quad (D.1)$$

where Q is the volumetric flux through a boundary cell (m^2/d), V_{tot} is the total volume of the model domain (m^2), ρ_{max} is the concentration at the top boundary which was set at 1078 kg/m^3, ρ_0 was the initial density of the groundwater in the domain (1000 kg/m^3), S_f is the specific storage in terms of fresh water head (d^{-1}), z_{max} the depth of the domain (m), and n the porosity (−). For the test with Δx, Δz was kept at 10 m; in testing Δz, Δx was kept at 10 m. As the density at the top boundary of the model was perturbed randomly, 10 simulations were started for each discretization, of which the minimum, maximum and mean of Ξ are plotted. It can be seen in Fig. D2 that there is some spread in Ξ, which is caused both by integration errors and differences between realizations. Furthermore a larger Δx causes a delay in the onset of free convection and causes a slower downward movement of fingers. However, all errors are unimportant on timescales larger than ~100 years, and thus also on our timescales of interest, which is over 1000 years.

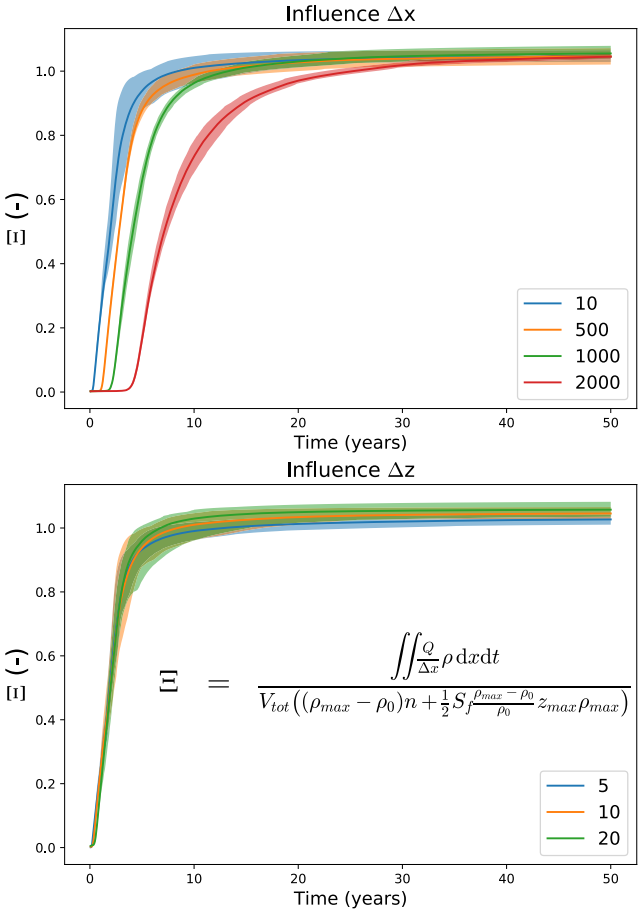

Fig. D2. Results of the test of the errors that are introduced in the free convection model by the large grid size.

References

Abd-Allah, A.M.A., Abdel Aal, M.H., Ghandour, A., 2012. Structural characteristics and tectonic evolution of the northwestern margin of the Nile Delta, Egypt. J. African Earth Sci. 68, 82–95. https://doi.org/10.1016/j.jafrearsci.2012.02.006.

Abdel-Fattah, M.I., 2014. Petrophysical characteristics of the messinian abu madi formation in the baltim east and north fields, offshore Nile delta, Egypt. J. Pet. Geol. 37 (2), 183–195. https://doi.org/10.1111/jpg.12577.

Abdel Aal, A., El Barkooky, A., Gerrits, M., Meyer, H., Schwander, M., Zaki, H., 2000. Tectonic evolution of the Eastern Mediterranean Basin and its significance for hydrocarbon prospectivity in the ultradeepwater of the Nile Delta. Lead. Edge 19 (10), 1086. https://doi.org/10.1190/1.1438485.

Aeschbach-Hertig, W., 2014. Radiokrypton dating finally takes off. Proc. Natl. Acad. Sci. U.S.A. 111 (19), 6856–6857. https://doi.org/10.1073/pnas.1405830111.

Andersen, M.S., Jakobsen, R., Nyvang, V., Christensen, F.D., Engesgaard, P., and Postma, D., 2007, Density-driven seawater plumes in a shallow aquifer caused by a flooding event - Field observations, consequences for geochemical reactions and potentials for remediation schemes, in GQ07: Securing Groundwater Quality in Urban and Industrial Environments (Proc. 6th International Groundwater Quality Conference held in Fremantle, Western Australia, 2–7 December 2007), pp. 2–7.

Bakker, M., Post, V., Langevin, C.D., Hughes, J.D., White, J.T., Starn, J.J., Fienen, M.N., 2016. Scripting MODFLOW model development using python and FloPy. Groundwater. https://doi.org/10.1111/gwat.12413.

Barrocu, G., Dahab, K., 2010. Changing climate and saltwater intrusion in the Nile Delta, Egypt. Taylor & Francis, pp. 11–25.

Bear, J., 1972. Dynamicsof Fluids in Porous Media, Dover Edition (1988). Dover Publications INC., New York.

Beaton, C.F., Edwards, D.K., Schlunder, E.U., 1987, Chapter 5.3.3, in Heat Exchanger Design Handbook, ed. E. U. Schlunder.

Bense, V.F., Gleeson, T., Loveless, S.E., Bour, O., Scibek, J., 2013. Fault zone hydrogeology. Earth-Sci. Rev. 127, 171–192. https://doi.org/10.1016/j.earscirev.2013.09.008.

Bredehoeft, J.D., Hanshaw, B.B., 1968. On the maintenance of anomalous fluid pressures: I. Thick sedimentary sequences. Bull. Geol. Soc. Am. 79, 1107–1122. https://doi.org/10.1130/0016-7606(1968)79[1107:OTMOAF]2.0.CO;2.

Bucx, T., Marchand, M., Makaske, B., van de Guchte, C. 2010, Comparative assessment of the vulnerability and resilience of 10 deltas – synthesis report., Delft-Wageningen.

Van Dam, R.L., Simmons, C.T., Hyndman, D.W., Wood, W.W., 2009. Natural free convection in porous media: First field documentation in groundwater. Geophys. Res. Lett. 36 (11), 1–5. https://doi.org/10.1029/2008GL036906.

Diab, M.S., Saleh, M.F., 1982. The hydrogeochemistry of the Pleistocene aquifer in the Nile Delta area, Egypt. Environ. Int. 7 (3), 221–230. https://doi.org/10.1016/0160-4120(82)90109-X.

Diab, M.S., Dahab, K.A., El-Fakharany, M.A., 1997. Impact of the Paleohydrogeological conditions on the groundwater quality in the Northern Part of the Nile Delta, Egypt. Egypt. J. Geol. 41 (2B), 779–796.

Domenico, P.A., Schwartz, F.W., 1990. Physical and Chemical Hydrogeology. John Wiley & Sons.

Eppelbaum, L., Kutasov, I., Pilchin, A., 2014. Thermal properties of rocks and density of fluids. In: Applied Geothermics. Springer-Verlag, Berlin Heidelberg, pp. 99–149.

FAO, 2005, Irrigation in Africa in figures: AQUASTAT survey. Box 1, Rome.
Farid, M., 1980, Nile Delta Groundwater Study, Cairo University.
Farouk, S., Ziko, A., Eweda, S.A., Said, A.E., 2014. Subsurface miocene sequence stratigraphic framework in the Nile Delta, Egypt. J. Afr. Earth Sci. 91, 89–109. https://doi.org/10.1016/j.jafrearsci.2013.12.010.
Fass, T., Cook, P.G., Stieglitz, T., Herczeg, A.L., 2007. Development of saline ground water through transpiration of sea water. Ground Water 45 (6), 703–710. https://doi.org/10.1111/j.1745-6584.2007.00344.x.
Fell, C.J., Hutchison, H.P., 1971. Diffusion coefficients for sodium and potassium chlorides in water. J. Chem. Eng. Data 16 (4), 427–429. https://doi.org/10.1021/je60051a005.
Garven, G., 1995. Continental scale groundwater flow and geologic processes. Annu. Rev. Earth Planet. Sci. 23, 89–117.
Gat, J.R., Levy, Y., 1978. Isotope hydrology of inland sabkhas in the Bardawil area, Sinai. Limnol. Oceanogr. 23, 841–850. https://doi.org/10.4319/lo.1978.23.5.0841.
GEBCO GEBCO Dataset Available from: http://www.gebco.net/data_and_products/gridded_bathymetry_data/gebco_30_second_grid/ 2014 accessed (05.10.16).
Geirnaert, W., Laeven, M.P., 1992. Composition and history of ground water in the western Nile Delta. J. Hydrol. 138 (1–2), 169–189. https://doi.org/10.1016/0022-1694(92)90163-P.
Gibson, R.E., 1958. The progress of consolidation in a clay layer increasing in thickness with time. Géotechnique 8, 171–182. https://doi.org/10.1680/geot.1958.8.4.171.
Goode, D.J., 1996. Direct simulation of groundwater age. Water Resour. Res. 32 (2), 289–296. https://doi.org/10.1029/95WR03401.
Griffioen, J., Verweij, H., Stuurman, R., 2016. The composition of groundwater in Palaeogene and older formations in the Netherlands. A synthesis. Netherlands J. Geosci. 95 (3), 349–372. https://doi.org/10.1017/njg.2016.19.
Guo, W., Langevin, C.D., 2002. User's Guide to SEAWAT: A computer program for simulation of three-dimensional variable-density ground-water flow. USGS, Tallahassee.
Han, D., Kohfahl, C., Song, X., Xiao, G., Yang, J., 2011. Geochemical and isotopic evidence for paleo-seawater intrusion into the south coast aquifer of Laizhou Bay, China. Appl. Geochem. 26 (5), 863–883. https://doi.org/10.1016/j.apgeochem.2011.02.007.
Hanor, J.S., 1994. Origin of saline fluids in sedimentary basins. Geol. Soc. Lon. Spec. Publ. 78 (1), 151–174. https://doi.org/10.1144/GSL.SP.1994.078.01.13.
Hanor, J.S., Mercer, J., 2011. Spatial variations in the salinity of pore waters in northern deep water gulf of mexico sediments: implications for pathways and mechanisms of solute transport. Geofluids 10, 83–93. https://doi.org/10.1002/9781444394900.ch7.
Helalia, A.M., 1993. The relation between soil infiltration and effective porosity in different soils. Agric. Water Manag. 24 (1), 39–47. https://doi.org/10.1016/0378-3774(93)90060-N.
Higgins, S.A., 2016. Review: advances in delta-subsidence research using satellite methods. Hydrogeol. J., 587–600 https://doi.org/10.1007/s10040-015-1330-6.
Jones, G.D., Whitaker, F.F., Smart, P.L., Sanford, W.E., 2002. Fate of reflux brines in carbonate platforms. Geology 30, 371–374. https://doi.org/10.1130/0091-7613(2002)030<0371:FORBIC>2.0.CO.
Kang, M., Jackson, R.B., 2016. Salinity of deep groundwater in California: water quantity, quality, and protection. Proc. Natl. Acad. Sci. U.S.A. 6. https://doi.org/10.1073/pnas.1600400113.
Kashef, A.-A.I., 1983. Salt-water intrusion in the nile delta. Groundwater 21 (2), 160–167. https://doi.org/10.1111/j.1745-6584.1983.tb00713.x.
Kirschbaum, M.A., Schenk, C.J., Carpentier, R., Klett, T.R., Brownfield, M.E., Pitman, J. K., Cook, T.A., Tennyson, M.E., 2010. Assessment of undiscovered oil and gas resources of the nile delta basin province eastern mediterranean. USGS Fact Sheet 3027, 1–4.
Kohfahl, C., Post, V., Hamann, E., Prommer, H., Simmons, C.T., 2015. Validity and slopes of the linear equation of state for natural brines in salt lake systems. J. Hydrol. 523, 190–195. https://doi.org/10.1016/j.jhydrol.2015.01.054.
Kooi, H., Groen, J., Leijnse, A., 2000. Modes of seawater intrusion during transgressions. Water Resour. Res. 36 (12), 3581–3589. https://doi.org/10.1029/2000WR900243.
Laeven, M.P., Hydrogeological Study of the Nile Delta and Adjacent Desert Areas in Egypt with emphasis on hydrochemistry and isotope hydrology, 1991, Amsterdam.
Langevin, C.D., Thorne Jr., D.T., Dausman, A.M., Sukop, M.C., Guo, W., 2007. SEAWAT version 4: a computer program for simulation of multi-species solute and heat transport. U.S. Geol. Surv. Techol. Methods B. 6, 39.
Levy, Y., 1977. The origin and evolution of brine in coastal sabkhas, Northern Sinai. J. Sediment. Petrol. 47 (1), 451–462.
Lindsay, J.F., Holliday, D.W., Hulbert, A.G., 1991. Sequence stratigraphy and the evolution of the Ganges-Brahmaputra delta complex. Am. Assoc. Pet. Geol. Bull. 75 (7), 1233–1254.
Lopez, D.L., Smith, L., 1995. Fluid flow in fault zones: analysis of the interplay of convective circulation and topographically driven groundwater flow. Water Resour. Res. 31 (6), 1489–1503.
Maczynska, A., 2014. Studies in African Archaeology vol 13: The Nile Delta as a centre of cultural interactions between Upper Egypt and the Southern Levant in the 4th millennium BC. Poznan Archaeological Museum and authors, Poznan.
Minderhoud, P.S.J., Erkens, G., Pham, V.H., Bui, V.T., Erban, L., Kooi, H., Stouthamer, E., 2017. Impacts of 25 years of groundwater extraction on subsidence in the Mekong delta, Vietnam. Environ. Res. Lett. 12 (6), 64006. https://doi.org/10.1088/1748-9326/aa7146.
Nashaat, M., 1998. Abnormally high formation pressure and seal impacts on hydrocarbon accumulations in the Nile Delta and North Sinai basins, Egypt. Abnorm. Press. Hydrocarb. Environ. AAPG. Mem. 70 (70), 161–180.
Neuzil, C.E., 2003. Hydromechanical coupling in geologic processes. Hydrogeol. J. 11 (1), 41–83. https://doi.org/10.1007/s10040-002-0230-8.
Nield, D.A., 1968. Onset of thermohaline convection in a porous medium. Water Resour. Res. 4 (3), 553–559. https://doi.org/10.1103/PhysRevLett. 94.205502.
Nield, D.A., Bejan, A., 2013. Convection in porous media. Fourth Edi, Springer, New York.
Nofal, E.R., Amer, M.A., El-Didy, S.M., Akram, M.F., 2015. Sea water intrusion in nile delta in perspective of new configuration of the aquifer heterogeneity using the recent stratigraphy data. J. Am. Sci. 11 (6), 567–570.
Park, J., Bethke, C.M., Torgersen, T., Johnson, T.M., 2002. Transport modeling applied to the interpretation of groundwater 36 Cl age. Water Resour. Res. 38 (5), 1–15. https://doi.org/10.1029/2001WR000399.
Person, M.A., Garven, G., 1994. A sensitivity study of the driving forces on fluid flow during continental rift evolution. Geol. Soc. Am. Bull. 106, 461–475.
Pierre, C., Bayon, G., Blanc-Valleron, M.-M., Mascle, J., Dupre, S., 2014. Authigenic carbonates related to active seepage of methane-rich hot brines at the Cheops mud volcano, Menes caldera (Nile deep-sea fan, eastern Mediterranean Sea) Catherine. Geo-Marine Lett. 34 (2), 253–267.
Post, V.E.A., Simmons, C.T., 2010. Free convective controls on sequestration of salts into low-permeability strata: insights from sand tank laboratory experiments and numerical modelling. Hydrogeol. J. 18 (1), 39–54. https://doi.org/10.1007/s10040-009-0521-4.
Post, V.E.A., Groen, J., Kooi, H., Person, M., Ge, S., Edmunds, W.M., 2013. Offshore fresh groundwater reserves as a global phenomenon. *Nature* 504 (7478), 71–78. https://doi.org/10.1038/nature12858.
Prasad, A., Simmons, C.T., 2005. Using quantitative indicators to evaluate results from variable-density groundwater flow models. Hydrogeol. J. 13 (5–6), 905–914. https://doi.org/10.1007/s10040-004-0338-0.
Riad, S., Abdelrahman, E.M., Refai, E., El-Ghalban, H.M., 1989. Geothermal studies in the Nile Delta, Egypt. J. Afr. Earth Sci. 9 (3–4), 637–649. https://doi.org/10.1016/0899-5362(89)90048-1.
Rizzini, A., Vezzani, F., Cococcetta, V., Milad, G., 1978. Stratigraphy and sedimentation of a Neogene-Quaternary section in the Nile Delta area (A.R.E.). Mar. Geol. 27 (3–4), 327–348. https://doi.org/10.1016/0025-3227(78)90038-5.
Samuel, A., Kneller, B., et al., 2003. Prolific deep marine slope channels of the Nile Delta, Egypt. Am. Assoc. Pet. Geol. Bull. 87 (4), 541–560. https://doi.org/10.1306/1105021094.
Schreiber, B. C., Hsü, K.J., 1980, Evaporites, in Developments in Petroleum Geology, p. 120.
Sefelnasr, A., Sherif, M., 2014. Impacts of seawater rise on seawater intrusion in the Nile Delta Aquifer Egypt. Groundwater 52 (2), 264–276. https://doi.org/10.1111/gwat.12058.
Sestini, G., 1989. Nile Delta: a review of depositional environments and geological history. Geol. Soc. London, Spec. Publ. 41 (1), 99–127. https://doi.org/10.1144/GSL.SP.1989.041.01.09.
Shackelford, C.D., Daniel, D.E., 1991a. Diffusion in saturated soil. I: background. J Geotechnol. Eng. 117 (3), 467–484.
Shackelford, C.D., Daniel, D.E., 1991b. Diffusion in saturated soil. II: results for compacted clay. J Geotech. Eng. 117 (3), 485–506. https://doi.org/10.1061/(ASCE)0733-9410(1991) 117:3(485).
Sharp, J.M., Domenico, P.A., 1976. Energy transport in thick sequences of compacting sediment. Bull. Geol. Soc. Am. 87 (3), 390–400. https://doi.org/10.1130/0016-7606(1976) 87<390:ETITSO>2.0.CO;2.
Shata, A.A., Hefny, K., 1995, Strategies for planning and management of groundwater in the Nile Valley and Nile Delta in Egypt. Working Paper Series No. 31-1, Strategic Research Program (SRP), NWRC-MPWWR, Cairo.
Shata, A. A. (1999), Contribution to the hydrogeology of the Nile delta region – Egypt, in Deltas, Modern & Ancient, p. 19, Cairo.
Sherif, M.M., Singh, V.P., Amer, A.M., 1988. A two-dimensional finite element model for dispersion (2D-FED) in coastal aquifers. J. Hydrol. 103 (1–2), 11–36. https://doi.org/10.1016/0022-1694(88)90003-0.
Simmons, C.T., Fenstemaker, T.R., Sharp, J.M., 2001. Variable-density groundwater flow and solute transport in heterogeneous porous media: approaches, resolutions and future challenges. J. Contam. Hydrol. 52 (1–4), 245–275. https://doi.org/10.1016/S0169-7722(01)00160-7.
Simmons, C.T., Kuznetsov, A.V., Nield, D.A., 2010. Effect of strong heterogeneity on the onset of convection in a porous medium: importance of spatial dimensionality and geologic controls. Water Resour. Res. 46 (9), 1–12. https://doi.org/10.1029/2009WR008606.
Stanley, D.J., Warne, A.G., 1993. Nile Delta: recent geological evolution and human impact. Science(80-) 260 (5108), 628–634. https://doi.org/10.1126/science.260.5108.628.
Stanley, J.D., Jorstad, T.F., 2006. Short contribution: buried canopic channel identified Near Egypt's nile delta coast with radar (SRTM) imagery. Geoarchaeology 21 (5), 503–514. https://doi.org/10.1002/GEA.
Sturchio, N.C. et al., 2004. One million year old groundwater in the Sahara revealed by krypton-81 and chlorine-36. Geophys. Res. Lett. 31 (5), 2–5. https://doi.org/10.1029/2003GL019234.
Summerhayes, C.P., Sestini, G., Misdorp, R., Marks, N., 1978. Nile Delta: nature and evolution of continental shelf sediments. Mar. Geol. 27, 43–65.

Taniguchi, M., Burnett, W.C., Cable, J.E., Turner, J.V., 2002. Investigation of submarine groundwater discharge. Hydrol. Process. 16 (11), 2115–2129. https://doi.org/10.1002/hyp.1145.

Trevisan, O.V., Bejan, A., 1990. Combined heat and mass transfer by natural convection in a vertical enclosure. Adv. Heat Transf. 20 (1), 315–352.

Vengosh, A., de Lange, G., Starinsky, A., 1998. Boron isotope and geochemical evidence for the origin of Urania and Bannock brines at the Eastern Mediterranean: Effect of water-rock interactions. Geochim. Cosmochim. Acta 62 (19–20), 3221–3228. https://doi.org/10.1016/S0016-7037(98)00236-1.

Vengosh, A., Spivack, A., Artzi, Y., Ayalon, A., 1999. Geochemical and boron, strontium, and oxygen isotopic constraints on the origin of the salinity in groundwater from the Mediterranean coast of Israel. Water Resour. Res. 35 (6), 1877–1894.

Verweij, J.M., 1999. Application of fluid flow systems analysis to reconstruct the post- carboniferous hydrogeohistory of the onshore and offshore Netherlands. Mar. Pet. Geol. 16, 561–579.

Voss, C.I., Wood, W.W., 1993. Synthesis of geochemical, isotopic and groundwater modeling analysis to explain regional flow in a coastal aquifer of southern Oahu, Hawaii. In: Mathematical Models and Their Applications to Isotope Studies in Groundwater Hydrology. IAEA, Vienna, pp. 147–178.

West, I.M., Ali, Y.A., Hilmy, M.E., 1979. Primary gypsum nodules in a modern sabkha on the Mediterranean coast of Egypt. Geology 7 (7), 354–358. https://doi.org/10.1130/0091-7613(1979) 7<354:PGNIAM>2.0.CO;2.

Wooding, R.A., Tyler, S.W., White, I., 1997. Convection in groundwater below an evaporating Salt Lake: 1. Onset of instability. Water Resour. Res. 33 (6), 1219. https://doi.org/10.1029/96WR03534.

WRI World Resources 2008 Data Tables 2008 Washington D.C.

Yechieli, Y., Kafri, U., Sivan, O., 2009. The inter-relationship between coastal sub-aquifers and the Mediterranean Sea, deduced from radioactive isotopes analysis. Hydrogeol. J. 17 (2), 265–274. https://doi.org/10.1007/s10040-008-0329-7.

Zheng, C., 2010, MT3DMS v5.3: Supplemental User's Guide, Tuscaloosa.

Zheng, C., and Wang, P.P., 1999, A Modular Three – Dimensional Multispecies Transport Model, Tuscaloosa.

Zimmermann, S., Bauer, P., Held, R., Kinzelbach, W., Walther, J.H., 2006. Salt transport on islands in the Okavango Delta: numerical investigations. Adv. Water Resour. 29 (1), 11–29. https://doi.org/10.1016/j.advwatres.2005.04.013.